

1 **IAPv4 ocean temperature and ocean heat content gridded**
2 **dataset**

3 Lijing Cheng^{1,11*}, Yuying Pan^{1,11}, Zhetao Tan^{1,11}, Huayi Zheng^{1,11}, Yujing Zhu^{1,11}, Wangxu
4 Wei^{1,11}, Juan Du¹, Huifeng Yuan^{2,11}, Guancheng Li³, Hanlin Ye¹, Viktor Gouretski¹,
5 Yuanlong Li^{4,11}, Kevin E. Trenberth^{5,6}, John Abraham⁷, Yuchun Jin^{4,11}, Franco Reseghetti⁸,
6 Xiaopei Lin⁹, Bing Zhang^{4,11}, Gengxin Chen^{10, 11}, Michael E. Mann¹², Jiang Zhu^{1,11}
7

8 ¹ Institute of Atmospheric Physics, Chinese Academy of Sciences, Beijing, China, 100029.

9 ² Computer Network Information Center, Chinese Academy of Sciences, Beijing, 100083.

10 ³ Eco-Environmental Monitoring and Research Center, Pearl River Valley and South China
11 Sea Ecology and Environment Administration, Ministry of Ecology and Environment,
12 PRC, Guangzhou 510611, China.

13 ⁴ Institute of Oceanography, Chinese Academy of Sciences, Qingdao, China.

14 ⁵ National Center for Atmospheric Research, PO Box 3000, Boulder, CO 80307, USA.

15 ⁶ University of Auckland, Auckland, New Zealand.

16 ⁷ University of St. Thomas, School of Engineering, 2115 Summit Ave., St Paul, MN
17 55105, USA.

18 ⁸ Istituto Nazionale di Geofisica e Vulcanologia, 40127, Bologna, Italy.

19 ⁹ Frontier Science Center for Deep Ocean Multispheres and Earth System and Physical
20 Oceanography Laboratory, Ocean University of China, Qingdao, China.

21 ¹⁰ State Key Laboratory of Tropical Oceanography, South China Sea Institute of
22 Oceanology, Chinese Academy of Sciences, Guangzhou, China

23 ¹¹ University of Chinese Academy of Sciences, Beijing, China.

24 ¹² Dept. of Earth and Environmental Science, University of Pennsylvania, Philadelphia PA,
25 USA
26

27 *Correspondence to:* Lijing Cheng (chenglij@mail.iap.ac.cn)

28

29 **Abstract.** Ocean observational gridded products are vital for climate monitoring, ocean
30 and climate research, model evaluation, and supporting climate mitigation and adaptation
31 measures. This paper describes the 4th version of the Institute of Atmospheric Physics
32 (IAPv4) ocean temperature and ocean heat content (OHC) objective analysis product. It
33 accounts for recent developments in quality control (QC) procedures, climatology, bias
34 correction, vertical and horizontal interpolation, and mapping and is available for the upper
35 6000 m (119 levels) since 1940 (more reliable after ~1957) for monthly and $1^\circ \times 1^\circ$
36 temporal and spatial resolutions. The IAPv4 is compared with the previous version, IAPv3,
37 and to the other data products, sea surface temperatures (SSTs), and satellite observations.
38 It has a slightly stronger long-term upper 2000 m OHC increase than IAPv3 for 1955-
39 2023, mainly because of newly developed bias corrections. IAPv4 OHC 0-2000 m trend is
40 also higher during 2005-2023 than IAPv3. The uppermost level of IAPv4 is consistent with
41 independent SST datasets. The month-to-month OHC variability for IAPv4 is desirably
42 less than IAPv3 and other OHC products investigated in this study, the trend of ocean
43 warming rate (i.e., warming acceleration) is more consistent with the net energy imbalance
44 at the top of the atmosphere than IAPv3, and the sea level budget can be closed within
45 uncertainty. The gridded product is freely accessible at:
46 <http://dx.doi.org/10.12157/IOCAS.20240117.002> for temperature data (Cheng et al.,
47 [2024a](http://dx.doi.org/10.12157/IOCAS.20240117.001)) and <http://dx.doi.org/10.12157/IOCAS.20240117.001> for ocean heat content data
48 (Cheng et al., 2024b).

49

50 **1. Introduction**

51 Observational gridded products are essential for understanding the ocean, the
52 atmosphere, and climate change; they support policy decisions and social-economy
53 developments (Abraham et al., 2022; Abraham and Cheng, 2022; Cheng et al., 2022a). For
54 instance, many of the climate indicators used in the Working Group I report of the 6th
55 Intergovernmental Panel on Climate Change (IPCC-AR6-WG1) are based on gridded
56 products (Gulev et al., 2021; IPCC, 2021), mainly because the raw oceanic data suffer
57 from inhomogeneous data quality and irregular and incomplete data coverage (Abraham et
58 al., 2013; Boyer et al., 2016; Cheng et al., 2022a; Meyssignac et al., 2019).

59 As more than 90% of the Earth's energy imbalance (EEI) in the past half-century has
60 accumulated in the ocean, increasing ocean temperature (T) and ocean heat content (OHC)
61 are essential climate variables for monitoring, understanding, and projecting climate
62 change (e.g., Rhein et al., 2013; Hansen et al., 2011; Trenberth, 2022; Trenberth et al.,
63 2009; von Schuckmann et al., 2020; Cheng et al., 2022). OHC also impacts air-sea and ice-
64 sea interactions and thus exerts a considerable influence over the other components of the
65 climate system. It provides critical feedback through energy, water, and carbon cycles
66 (Cheng et al., 2022a; Trenberth, 2022; von Schuckmann et al., 2016). Substantial changes
67 in ocean temperatures also profoundly impact ocean biogeochemical processes and
68 ecosystems and are critical for ocean health and human society (Bindoff et al., 2019;
69 Cheng et al., 2022a).

70 Many gridded T/OHC datasets have been produced by independent groups, and most
71 of them are updated annually or more frequently (Cheng et al., 2022a; Good et al., 2013;
72 Hosoda et al., 2008; Ishii et al., 2017; Levitus et al., 2012; Li et al., 2017; Meyssignac et
73 al., 2019; Roemmich and Gilson, 2009). Most widely-used products are at $1^\circ \times 1^\circ$
74 horizontal resolution and monthly temporal resolution from near-surface to at least 2000 m
75 depth. Some products utilize all available *in situ* observations and span at least half a
76 century, prominent examples being the data products compiled by the Institute of
77 Atmospheric Physics (IAP) (Cheng and Zhu, 2016; Cheng et al., 2017) from 1940-present;
78 Japan Meteorological Agency (JMA) (Ishii et al., 2017) from 1955-present; National
79 Centers for Environmental Information (NCEI), National Oceanic and Atmospheric
80 Administration (NOAA) from 1950-present (Levitus et al., 2012); and University of
81 California since 1949 (Bagnell and DeVries, 2021). As Argo data has achieved near-global
82 upper 2000 m open ocean coverage since ~2005, many Argo-based or Argo-only gridded
83 products are available. Examples include gridded products from SCRIPPS after 2004
84 (Roemmich and Gilson, 2009); China Argo Real-time Data Center since 2005 (Li et al.,
85 2017); and Copernicus since 2005 (von Schuckmann and Le Traon, 2011). These products
86 usually span from ~2005 to the present for the upper ~2000 m. These data benefit from the
87 high quality of Argo data but are not fully resolving polar regions, shallow waters, and
88 regions with complex topography.

89 In 2016, the IAP group provided its first gridded product for the upper 700 m ocean
90 (Cheng and Zhu, 2016) by merging all available observations since 1960. With a revised
91 mapping method and a thorough evaluation process with synthetic observations, an update

92 (IAP version 3, IAPv3) became available in 2017 for the upper 2000 m ocean with data
93 since the 1950s (Cheng et al., 2017). The IAPv3 has supported scientific research, climate
94 assessment reports, and monitoring practices (Bindoff et al., 2019; Gulev et al., 2021;
95 WMO, 2022).

96 After the release of IAPv3, there has been progress with observation data quality
97 control and new/updated techniques for temperature data processing and reconstruction.
98 For example, Gouretski et al. (2022) found that old Nansen cast bottle data contained
99 systematic biases that impacted the T/OHC data before 1990. Revisions are also available
100 to the bias corrections for the Mechanical Bathythermographs (MBT) and eXpendable
101 Bathythermographs (XBT) data (Cheng et al., 2014; Gouretski and Cheng, 2020), mainly
102 impacting the data within 1940–2005. Tan et al. (2023) developed a new quality-control
103 system that advances the detection of outliers after accounting for the non-Gaussian
104 distribution of local temperatures in determining the local climatological range. The impact
105 of inhomogeneous vertical resolution of temperature profiles has been recognized
106 previously (Cheng and Zhu, 2014) and received more attention recently (Li et al., 2020)
107 with a new vertical interpolation approach (Barker and McDougall, 2020). Upgrading the
108 product with new developments is important to better support the ocean/climate research
109 and climate assessments.

110 This manuscript discusses the revisions to the IAP ocean objective analysis product
111 (IAPv4) since the publication of the IAPv3 (Cheng et al., 2017). The data and methods are
112 introduced in Section 2 and the results are presented in Section 3, with analyses of the
113 character of the IAPv4 on regional and global scales and at various time scales. The EEI
114 and sea level budgets based on the new data product are also investigated. A summary and
115 discussion are provided in Section 4, with some remaining issues and outlooks being
116 discussed.

117

118 **2. Data and Methods**

119 **2.1 Data source**

120 The majority of the *in situ* measurements used to create the data product come from
121 the World Ocean Database (WOD), downloaded in September 2023. Data from all
122 instrument types are used, including XBTs (Goni et al., 2019), Argo (Argo 2000),
123 Conductivity/Temperature/Depth profilers (CTDs), MBTs, bottles, moorings, gliders,
124 Animal Borne Ocean Sensors (McMahon et al., 2021) and others (Boyer et al., 2018) (Fig.

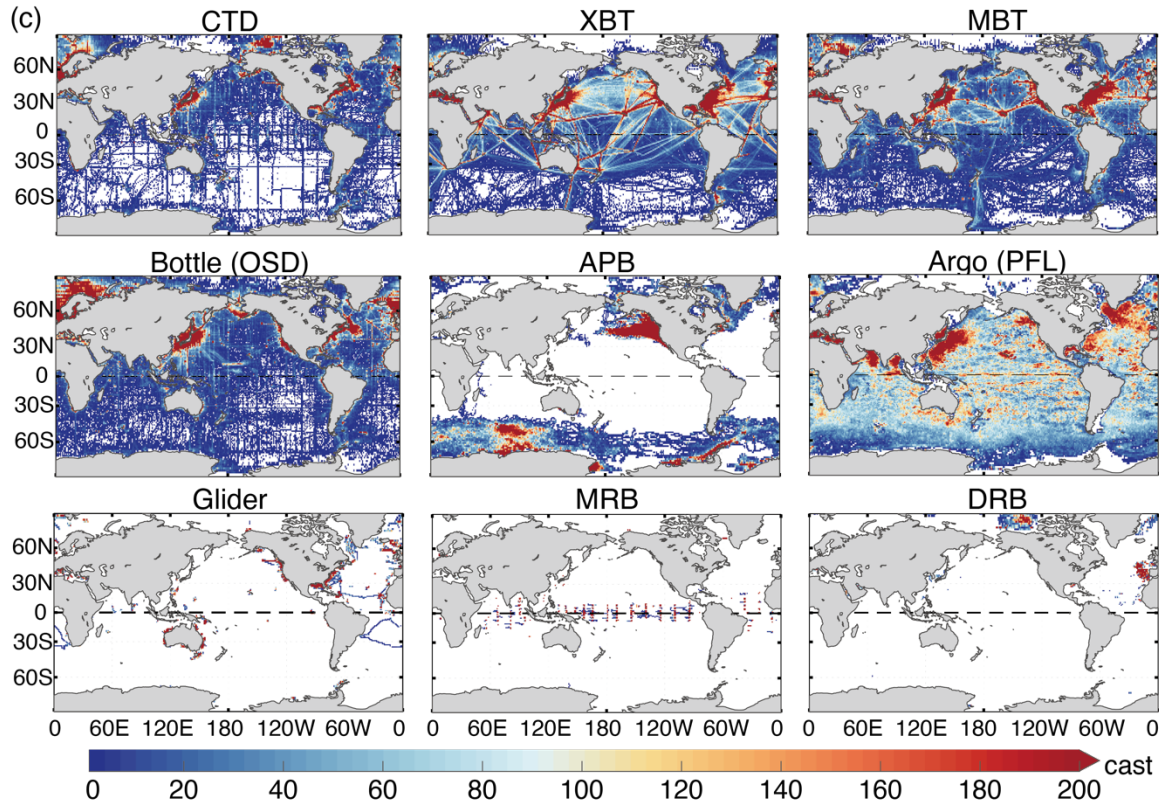
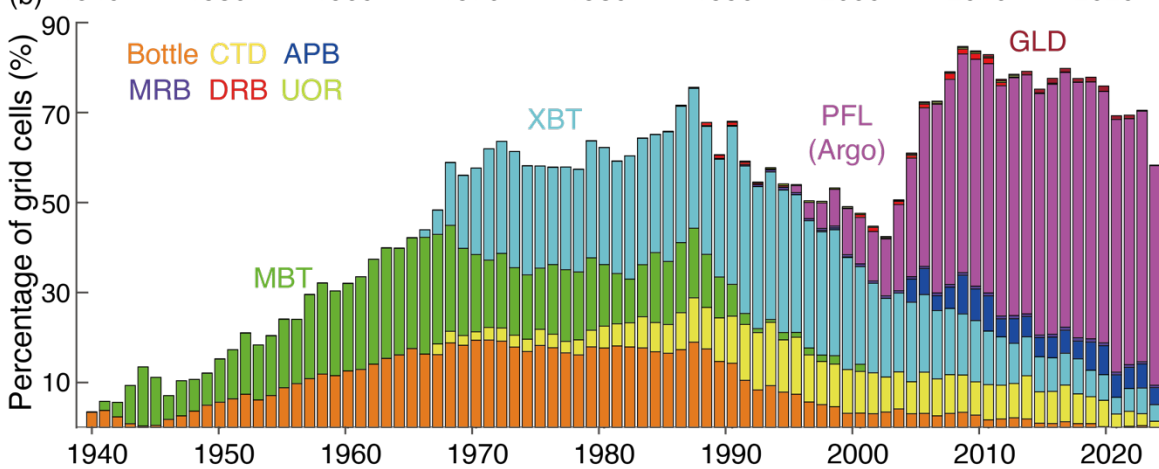
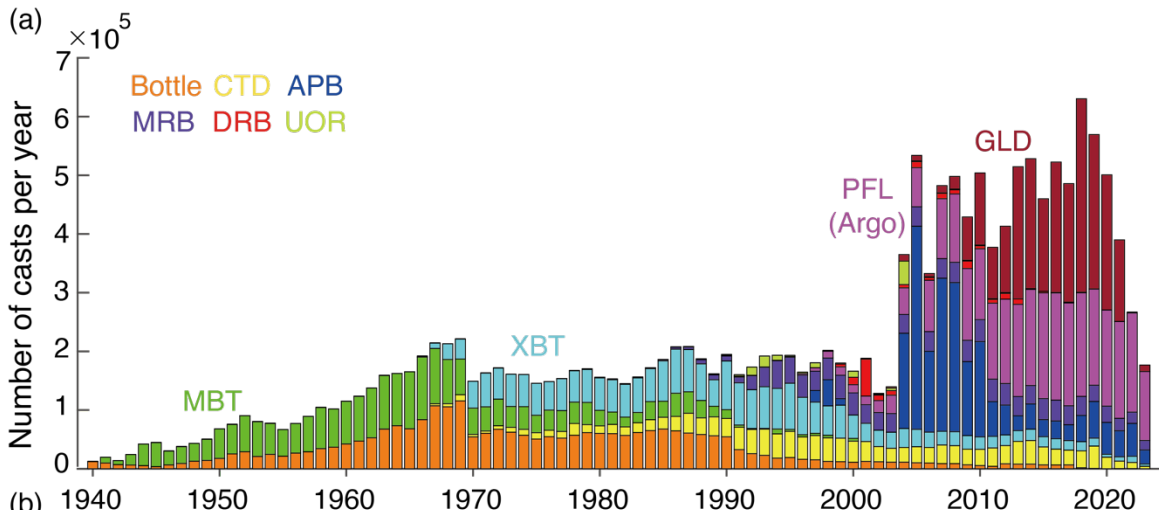
125 1). There is a total of 17,634,865 temperature profiles from January 1940 to September
126 2023 (Fig. 1a). MBT, XBT, Nansen Bottle and CTD data are the major instruments before
127 2000 (Fig. 1a, b). The spatial coverage of these data increased to >30% in 1960 and >70%
128 in the late 1960s for $1^\circ \times 1^\circ \times 1$ -year resolution. After 2005, there is a huge number of
129 GLD and APB data, and as they are mainly distributed in the polar regions (APB) and
130 coastal regions (GLD) (Fig. 1a), their spatial coverage is usually less than 5% for $1^\circ \times 1^\circ \times$
131 1 year resolution. By contrast, the Argo data cover most of the global open ocean since
132 ~2005 (Fig. 1b).

133 Argo data are processed following the recommendations of the Argo community.
134 Adjusted data are used where applicable. Both Delayed- and Real-Time Argo data have
135 been incorporated in IAPv4. As Real-Time Argo data have only passed automated, simple
136 QC tests in real-time, these data may still contain temperature, pressure, and salinity values
137 affected by unknown errors. However, through a sensitivity study, Cheng (2024) indicated
138 that including Real-Time Argo data does not bias the OHC calculation for the IAP
139 analysis. Nevertheless, IAP data are updated frequently (every 1-3 months): each time the
140 updated Argo data is used, the T/OHC fields are recalculated following the
141 recommendation by the Argo group (Wong et al., 2020). The data from the Argo floats in
142 the “grey list” have been removed from the calculation (<https://data-argo.ifremer.fr/>).

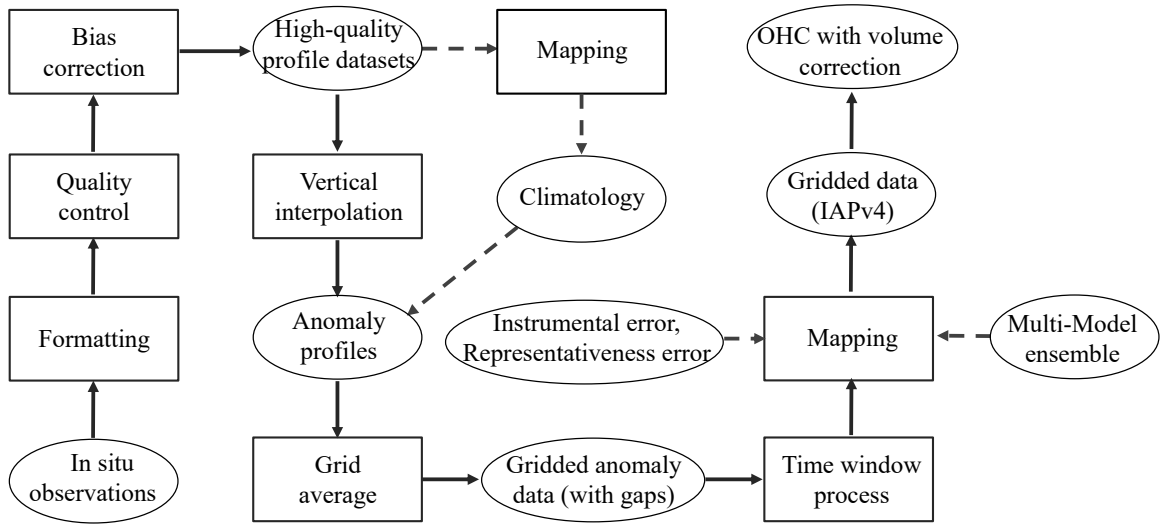
143 To complement the WOD with relatively less data in the Arctic and coastal regions of
144 the Northwest Pacific, this presented product also uses data from other sources. The
145 majority of these data are from the Chinese Academy of Sciences Ocean Science Data
146 Center (Zhang et al., 2024), and some data are rescued from the old documents of marine
147 surveys. All these data will be publicly available. There are a total of 85,990 additional
148 temperature profiles, about 0.50% of the data, which is expected to improve the
149 reconstruction in these data-sparse regions (compared with IAPv3 and other products).

150 The *in situ* data have been processed as described in a flow chart in Figure 2. In the
151 following sections, the key techniques of data processing are introduced.

152



154 **Figure 1: (a) Yearly number of temperature casts for different instruments; (b)**
 155 **percentage coverage (%) of ocean data for each instrument, calculated as the ratio**
 156 **between the number of $1^\circ \times 1^\circ \times 1$ year grid cells observed by each instrument and**
 157 **the total number of ocean grids; (c) number of subsurface temperature casts in 1-**
 158 **degree grid boxes from 1940 to 2023 collected by different instruments: CTD**
 159 **(Conductivity/Temperature/Depth), XBT (eXpendable BathyThermographs), MBT**
 160 **(Mechanical BathyThermograph), Bottle, APB (Animal mounted Pinniped Borne), PFL**
 161 **(Profiling Floats, i.e. Argo), GLD (Glider), MRB (Moored Buoy), and DRB (Drifting**
 162 **Buoy).**
 163



164
 165 **Figure 2: Flow chart of the IAP data reconstruction processes from the raw *in situ***
 166 **observations to gridded data (IAPv4) and OHC estimates.** The ellipses indicate the data
 167 (including data for error estimates), and the rectangle boxes show the techniques used to
 168 process the data.

169

170 2.2 Data quality control

171 The quality control (QC) procedure aims to identify spurious measurements (including
 172 outliers) and data with incorrect metadata through a set of quality checks and ensures the
 173 quality of the *in situ* dataset (Tan et al., 2022). There is growing evidence that QC is
 174 critical for accurate temperature/OHC reconstruction, as shown by Tan et al., (2023) where
 175 two different QC systems produced a difference of approximately 15 % (~7 %) in the OHC
 176 0-2000 m trend from 1955 to 1990 (2005-2021). Unfortunately, the impact of QC on OHC

177 estimates has not been evaluated in previous community-assessments on T/OHC
178 uncertainty (Boyer et al., 2016; Lyman et al., 2010). In this study, the QC procedure
179 follows the CAS-Ocean Data Center (CODC) Quality Control system, named CODC-QC
180 (Tan et al., 2023), where only the “good” data (flag=0) are used.

181 The CODC-QC system (Tan et al., 2023) has the following strengths, which make it
182 particularly suitable for T/OHC reconstruction:

183 1) A new local climatological range is defined in this CODC-QC system to identify
184 the outliers. Unlike many existing QC procedures, no assumption is made of a Gaussian
185 distribution law in the new approach, as the oceanic variables (e.g., temperature and
186 salinity) are typically skewed. Instead, the 0.5 % and 99.5 % quantiles are used as
187 thresholds in CODC-QC to define the local climatological parameter ranges.

188 2) Local climatological ranges change with time to account for the long-term trends of
189 ocean temperature accompanied by more frequent extreme events (e.g., Oliver et al., 2018;
190 Sun et al., 2023). Previously, the use of the static local ranges tended to remove too many
191 “extreme values” (at the tails of the temperature distributions) associated with climate
192 change in recent years that were actually real, leading to a QC-procedure related bias in the
193 gridded dataset and OHC estimate (Tan et al., 2023).

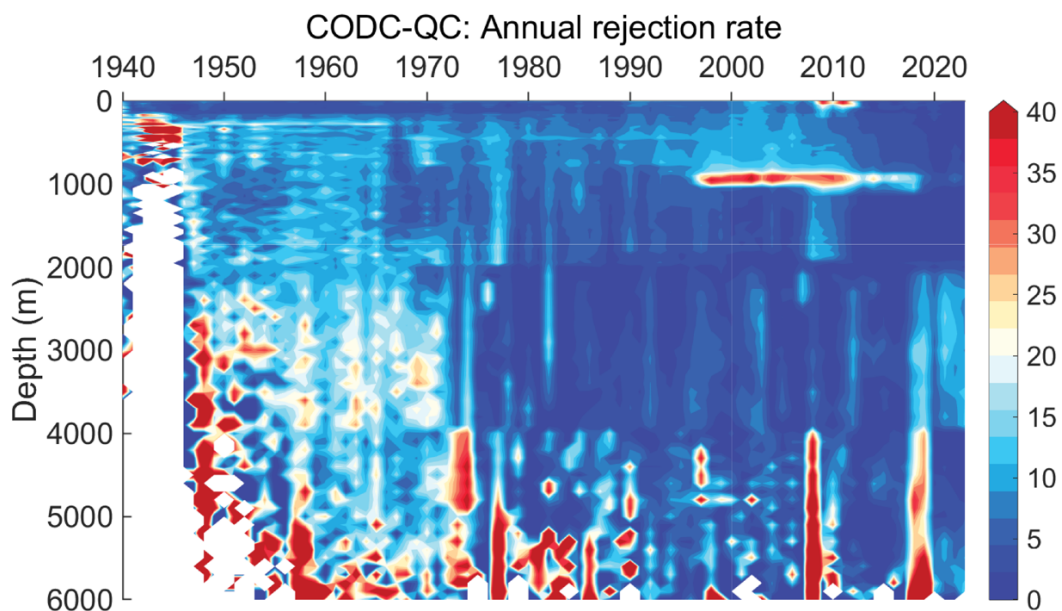
194 3) In addition, local climatological ranges for the vertical temperature gradient are
195 constructed to account for the variability of ‘vertical shape’, increasing the ability of the
196 scheme to identify spurious profiles.

197 4) The QC procedure is instrument-specific, accounting for characteristics inherent to
198 particular instrumentation types. For example, XBT digital recording systems are allowed
199 to continue to record beyond the rated terminal depth suggested by manufacturers (T7/DB
200 probes below 760 m; T4/T6 below 460 m; T5 below 1830 m). Below the rated maximum
201 depth, the XBT wire often breaks, leading to a characteristic change in recorded
202 temperature values. The new QC procedure effectively identifies such profiles.

203 5) The thorough evaluation of the QC procedure performance and the application of
204 the QC procedure to the manually QC-ed datasets (Thresher et al., 2008; Gouretski and
205 Koltermann, 2004) demonstrated the effectiveness of the proposed scheme in removing
206 spurious data and minimizing the percentage of mistakenly flagged good data.

207 Being applied to the entire temperature profile dataset the CODC-QC procedure
208 identifies 6.22 % of all temperature measurements as outliers. The rejection rates
209 (definition follows Tan et al., 2023) vary among instrumentation types (3.73 % for CTD,

210 1.97 % for Argo, 12.06 % for XBT, 4.93 % for MBT, 6.54 % for bottle, 5.92 % for APB,
 211 4.54 % for DRB, 2.55 % for MRB). The overall percentage of outliers decreases over time
 212 from ~5 % in the 1940s to ~2.5 % in the 2020s, reflecting the progressive improvement of
 213 the instrumentation (Fig. 3). A rejection rate maximum (~12 %) during 2000~2010 is
 214 linked to the XBT data, which are especially abundant in the 800–1100m layer and are
 215 characterized by higher rejection rate below the maximum depth (Tan et al., 2023). The
 216 generally higher rejection rate below 4000 meters is related to the gross errors (such as
 217 measurements cooler than -2°C, big spikes, etc.) and the occurrence of the constant values
 218 (recorded values don't change with depth). For example, the higher rejection rate within
 219 2008-2009 below 4000 meters is because of the gross errors in the CTD data.



220
 221 **Figure 3: The rejection rate (%) after CODC-QC as a function of calendar year and**
 222 **depth.**
 223

224 2.3 Bias correction

225 It is well known that data from several instrument types can exhibit biases both in
 226 temperature and depth. Temperature profiles obtained using XBTs and MBTs provide an
 227 example of biased data, especially because of uncertainties in the depth of measurement.
 228 Gouretski and Koltermann (2007) demonstrated their significant impact on the magnitude
 229 and variability of the global OHC estimates. That study triggered a series of publications
 230 where different bias correction schemes have been suggested for XBT (Gouretski and

231 Reseghetti, 2010; Abraham et al., 2013; Cheng et al., 2016; Levitus et al., 2009; Wijffels et
232 al., 2008), MBT (Gouretski and Cheng 2020; Levitus et al., 2009) and other instruments
233 (Fig. 2). In the compilation of IAPv4, newly developed bias correction schemes are
234 applied.

235 The XBT temperature bias was found to be generally positive, as large as ~ 0.1 °C
236 before 1980 on the global 0–700 m average, diminishing to less than 0.05 °C after 1990
237 (Gouretski and Koltermann 2007; Wijffels et al., 2008). Here, we use an updated XBT bias
238 correction scheme (Cheng et al., 2014) to correct both depth and temperature biases in
239 XBT data, following the community recommendation (Cheng et al., 2016; Goni et al.,
240 2019). The depth and temperature biases depend on ocean temperature, probe type, and
241 time. An inter-comparison among several correction schemes rated the CH14 scheme the
242 most successful (Cheng et al., 2018). Using XBT and collocated CTD data, we updated the
243 CH14 scheme by re-calculating bias corrections between 1966-2016 and extending them
244 for the years 2017 to 2023.

245 Comparison with collocated reference CTD profiles recently revealed significant
246 biases in the old hydrographic profiles obtained by means of Nansen bottle casts
247 (Gouretski et al., 2022). Both depth and temperature measurements of bottle casts were
248 found to be biased, and the proposed correction scheme was also implemented in IAPv4.
249 The thermal bias is related to the time needed to bring the mercury thermometers in
250 equilibrium with the ambient temperature after the completion of the hydrographic cast.
251 The depth bias indicates an overestimation of the bottle depth due to the wire's deviation
252 from the vertical position and is mostly related to the hydrographic casts where the
253 thermometrical method of sample depth determination was not used. The correction
254 scheme includes a constant thermal bias of -0.02 °C and a depth- and time-variable depth
255 bias.

256 The MBT bias is as large as 0.28 °C before 1980 for the global average and reduces to
257 less than 0.18 °C after 1980 for the 0–200 m average. IAPv3 used Ishii and Kimoto, (2009)
258 (IK09) scheme to correct MBT bias, while a new scheme proposed by Gouretski and
259 Cheng, (2020) (GC20) is adopted in IAPv4. This shift is made because our assessment
260 indicates the under-correction of MBT bias by the IK09 scheme within the upper 120 m
261 and over-correction in the deeper layer, whereas GC20 corrects both depth and temperature
262 biases. GC20 also found the MBT bias to be country-dependent, explained in terms of
263 different instrumentation characteristics and working procedures. Therefore, the time-

264 varying bias corrections are applied separately for the MBT profiles obtained by ships
265 from the United States, Soviet Union/Russia, Japan, Canada, and Great Britain. Data from
266 all other countries are corrected using a globally averaged correction.

267 Finally, thermal biases were recently reported for the data obtained by different kinds
268 of data loggers attached to marine mammals (APB). Gouretski et al. (2024) analysed
269 temperature profiles obtained between 2004 and 2019 in the high and moderate latitudes of
270 both hemispheres. Comparison with the collocated reference CTD and Argo float data
271 revealed a systematic negative thermal offset (average value -0.027 °C) for mammal
272 temperature profiles from SRDL (satellite-related data loggers). For the less accurate data
273 from TDR (Temperature-Depth-Recorders), the comparison revealed a small positive
274 temperature bias of 0.02 °C and the depth (pressure) bias indicating depth overestimation.

275

276 **2.4 Climatology**

277 For IAP and other data product generators, horizontal interpolation (mapping) is
278 applied on a temperature anomaly field after removing a monthly climatology; thus, a pre-
279 defined climatology field with an annual cycle is mandatory (Fig. 2). The accuracy of the
280 climatology field is one of the key sources of uncertainty in reconstruction because the
281 error in climatology will propagate into the anomaly field, impact the spatial dynamical
282 consistency, and the accuracy of the reconstruction (Cheng and Zhu, 2015; Lyman and
283 Johnson, 2014; Boyer et al., 2016).

284 In IAPv4, the adjusted mapping procedure (see below) has been applied to reconstruct
285 the climatology field (Table 1). The merit of using IAP mapping for climatology is its
286 ability to better represent the spatial anisotropy of temperature variability (non-Gaussian
287 distribution). Unlike IAPv3, where the 1990–2005 reference period was used, IAPv4 uses
288 data between 2006 and 2020 to construct 12 monthly climatologies, taking advantage of
289 more reliable data combined with better and more homogeneous spatial and temporal
290 coverage in the last two decades (Table 1). Following the recommendation in Cheng and
291 Zhu, (2015), a relatively short period of 15-year is used because climatology constructed
292 with longer period of data will result in different baselines at different locations (i.e., the
293 baseline shifted to earlier years in the middle latitudes of the North Hemisphere and the
294 baseline shifted to more recent years in the Southern Hemisphere) and this inconsistency
295 will violate the spatial structure of the anomaly field (Cheng and Zhu, 2015). Recent

296 developments from other groups, such as Li et al., (2022), include the choice of a short-
297 period climatology.

298 IAPv4 used an 800 km influencing radii in climatology reconstruction, smaller than
299 the 20° for IAPv3, to more properly account for the rapid change of temperatures with
300 distance. There is a trade-off between data availability and the size of the influence radius.
301 Using radii smaller than 500 km does not ensure a global fractional coverage (defined as
302 the fraction of the total ocean area obtained by the mapping method) because of data
303 sparseness (Cheng, 2024). As our tests suggest, using 500~800 km results in very similar
304 reconstructions of climatology, therefore, 800 km is adopted.

305

306 **2.5 Vertical interpolation**

307 The vertical resolution of ocean temperature profiles changed dramatically over time
308 associated with instrument evolution and the increase of data storage capability. For
309 instance, the global mean vertical resolution at 500 m level changed from ~100 m in the
310 1960s to less than 10 m during the 2010s (Li et al., 2020). Vertical interpolation of the raw
311 profiles on standard levels is a critical process (Fig. 2): Cheng and Zhu (2014) indicated
312 that the use of linear or spline vertical interpolation methods can bias the temperature
313 reconstruction and OHC estimation (Barker and McDougall, 2020; Li et al., 2020; Li et al.,
314 2022). IAPv3 used the (Reiniger and Ross, 1968) (RR) method. Recently, Barker and
315 McDougall (2020) proposed a new approach using multiple Piecewise Cubic Hermite
316 Interpolating Polynomials (PCHIPs) to minimize the formation of unrealistic water masses
317 by the interpolation procedure.

318 Because the largest difference between interpolation methods is found mostly for the
319 low-resolution profiles (e.g., old Nansen casts), in practice, extremely low vertical
320 resolution profiles had to be removed to reduce the uncertainty in interpolation. In IAPv4,
321 this procedure is optimized compared to IAPv3, and only parts of profiles with a sufficient
322 vertical resolution are used. The thresholds for the vertical resolution are set by 50 m in the
323 upper 200m, 200m between 200 m and 1000 m, 500 m between 1000 m and 2000 m, and
324 600m between 2000 m and 6000 m. As no interpolation method can adequately interpolate
325 temperature for the vertical resolution beyond these thresholds, interpolation is not
326 performed in such cases to avoid errors (these extreme low-resolution data are not used in
327 further processing). Under this limitation for IAPv4, we still apply the RR method for
328 temperature profiles.

329 Finally, IAPv4 extends the set of standard vertical levels with a total of 119 levels
330 from 1 m to 6500 m (79 levels within the upper 2000 m) compared to 41 levels in IAPv3
331 between 1 m and 2000 m (Table 1). The increase in vertical resolution is critical for
332 accurately representing the mixed layer, as investigated below.

333

334 **2.6 Grid average and mapping**

335 The anomaly profiles are obtained by subtracting the monthly mean climatology from
336 the vertically interpolated profiles. These anomalies are then averaged (arithmetic mean)
337 into a $1^\circ \times 1^\circ$ grid at each standard level ($1^\circ \times 1^\circ$ gridded average field) (Fig. 2). Due to the
338 general data sparsity, variable time windows (larger than one month) are used for monthly
339 reconstructions to ensure a truly global analysis (Supplementary Table 1). This process
340 takes advantage of the larger persistence of anomalies (generally smaller monthly and
341 inter-annual variability) in the deep ocean than in the upper ocean and thus is physically
342 grounded. Specifically, after 2005, data within a three-month window are merged to
343 provide a monthly reconstruction for each layer of the upper 1950 m. Before 2005, a time-
344 varying and depth-varying time window is used, and it is generally smaller in the upper
345 ocean and wider in the deeper ocean (Supplementary Table 1). Below 2000 m, a 5-year
346 (60-month) window is adopted. The use of a time window will reduce the monthly
347 variance compared to other datasets, which is likely too high compared with independent
348 Earth's Energy Imbalance data at the top of the atmosphere (Trenberth et al., 2016).

349 Mapping interpolates the gridded (e.g., box-averaged) observations horizontally into a
350 spatially complete map (Fig. 2) because not all $1^\circ \times 1^\circ$ boxes are filled with data. (Fig. 2).
351 IAPv4 adopted a similar mapping approach (Ensemble Optimal Interpolation with dynamic
352 ensemble: EnOI-DE) as in IAPv3 introduced in Cheng and Zhu (2016) and Cheng et al.,
353 (2017) but with the following modifications:

354 1) the largest influence radius has changed from 20° in the upper 700 m (25° at 700–
355 2000 m) in IAPv3 to 2,000 km in the upper 700 m (2,500 km at 700–6000 m) in IAPv4, to
356 account for the reduced distance between two longitudes from tropics to the polar regions.
357 This change mainly helps to improve the reconstruction in the high-latitude regions;

358 2) The three iterative runs are taken to effectively bring in different scales of
359 variability with influencing radius changing from 2,000 km (2,500 km at 700–6000 m) to
360 800 km and 300 km, respectively, based on the tests presented in Cheng and Zhu (2016)
361 and Cheng et al., (2017);

362 3) For each month, IAPv3 used 40 model simulations (historical runs) from the
363 Coupled Model Intercomparison Project phase 5 (CMIP5) to provide a flow-dependent
364 ensemble, which is then constrained by observations to provide optimized spatial
365 covariance. IAP mapping uses model-based covariance because we argue that spatial
366 covariance can never be satisfactorily parametrized by some simple basic functions (such
367 as Gaussian) given its complexity. With model-based, flow-dependent, and dynamically-
368 consistent covariance, the IAP mapping provides a more realistic reconstruction than other
369 approaches based on Gaussian-based parameterized covariance, as evaluated by many
370 studies (Cheng et al., 2017; Cheng et al., 2020; Dangendorf et al., 2021; Nerem et al.,
371 2018).

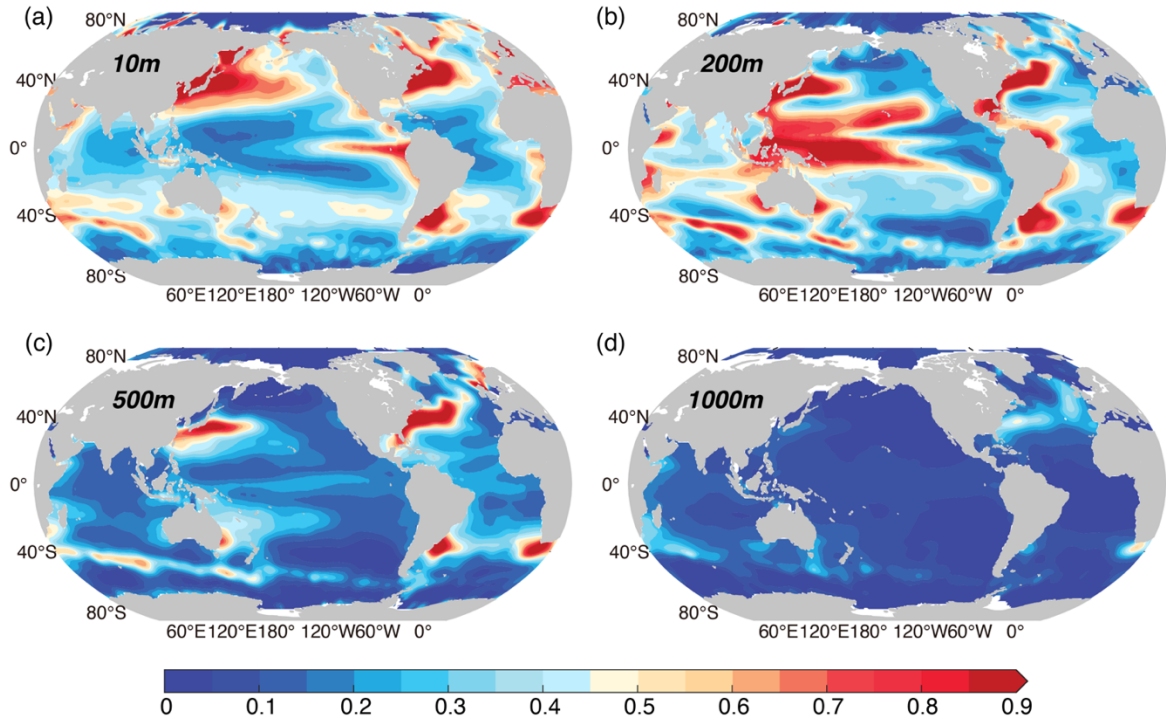
372 4) The observation error variance (\mathbf{R}), which represents the error of the observations,
373 is updated in IAPv4 as follows. \mathbf{R} consists of both the instrumental error (\mathbf{R}_e) due to
374 inaccuracy and the representativeness error (\mathbf{R}_r) due to the need to represent the spatial (at
375 1° by 1° and 1 m standard grid depths) and temporal (1 month) averages from a limited
376 numbered of observations (Cheng and Zhu, 2016):

$$377 \quad \mathbf{R} = \mathbf{R}_e + \mathbf{R}_r = (\sum_1^M \mathbf{E}i)/M + \sigma^2/M,$$

378 where M observations exist for a given grid cell. $\mathbf{E}i$ is the instrument's precision for
379 each individual observation, assuming random error (the basic assumption is that after bias
380 correction, the systematic errors can be eliminated). \mathbf{R}_e in each grid cell is set to the mean
381 of the typical precision of the different instruments contributing data in the cell, which is
382 set according to IQuOD (International Quality-Controlled Ocean Database) specification
383 (Cowley et al., 2021). σ^2 represents the variance of the various temperature measurements
384 against the monthly mean value. The data from 2005 to 2022 are used to calculate σ^2 in
385 each grid because of greater data abundance and quality compared to earlier times.

386 As the representativeness error (\mathbf{R}_r) is expected to be flow-dependent (i.e., the error is
387 expected to be higher in areas with a large gradient of the flow speed and regions of higher
388 variability), more observations are required to represent the mean value. Figure 4 shows a
389 larger variance (σ^2) in the boundary-current regions and near the Antarctic Circumpolar
390 Current (ACC) in the upper ocean (e.g., 10 m, 200 m, 500 m). At 200 m, it shows a larger
391 σ^2 in the Western Pacific Ocean, corresponding to the large thermocline variations at this
392 layer. Below 1000 m, larger σ^2 along the ACC frontal regions and in the North Atlantic
393 Ocean occur because of a stronger mixing and convection in these regions.

394 The uncertainty in the derived gridded reconstruction is also based on the EnOI
 395 framework formulated by Cheng and Zhu, (2016). The uncertainty accounts for
 396 instrumental, sampling and mapping errors. Other error sources, including the choice of
 397 climatology, vertical interpolation, bias corrections, and QC, are not considered in this
 398 uncertainty estimate. Therefore, a more thorough uncertainty quantification method is
 399 needed, and this is under development in a separate study.



400

401 **Figure 4: Variance (σ^2) of ocean temperature at several representative layers. (a)**

402

10 m, (b) 200 m, (c) 500 m and (d) 1000 m. The unit is $^{\circ}\text{C}^2$.

403

404

Table 1. General information on IAPv4 and IAPv3 data products.

	IAPv3	IAPv4
Horizontal resolution	Global ($1^{\circ} \times 1^{\circ}$)	Global ($1^{\circ} \times 1^{\circ}$)
Vertical levels	41 levels from 1 m to 2000 m (1, 5, 10, 20, 30, 40, 50, 60, 70, 80, 90, 100, 120, 140, 160, 180, 200, 250, 300, 350, 400, 450, 500, 550, 600, 650, 700, 750, 800, 850, 900, 1000, 1100, 1200, 1300, 1400, 1500, 1600, 1700, 1800, 2000)	119 levels from 1 m to 6000 m (1, 5, 10, 15, 20, 25, 30, 35, 40, 45, 50, 55, 60, 65, 70, 75, 80, 85, 90, 95, 100, 110, 120, 130, 140, 150, 160, 170, 180, 190, 200, 220, 240, 260, 280, 300, 320, 340, 360, 380, 400, 425, 450, 475, 500, 525, 550, 575, 600, 625, 650, 675, 700, 750, 800, 850, 900, 950, 1000, 1050, 1100, 1150, 1200,

		1250, 1300, 1350, 1400, 1450, 1500, 1550, 1600, 1650, 1700, 1750, 1800, 1850, 1900, 1950, 2000, 2100, 2200, 2300, 2400, 2500, 2600, 2700, 2800, 2900, 3000, 3100, 3200, 3300, 3400, 3500, 3600, 3700, 3800, 3900, 4000, 4100, 4200, 4300, 4400, 4500, 4600, 4700, 4800, 4900, 5000, 5100, 5200, 5300, 5400, 5500, 5600, 5700, 5800, 5900, 6000)
Time period and resolution	1940–2022 (reliable data after 1955), monthly	1940–present (reliable data after 1955), monthly
Quality-control	WOD (Garcia et al., 2018)	CODC-QC (Tan et al., 2023)
Vertical interpolation	RR (Reiniger and Ross, 1968) interpolation	RR (Reiniger and Ross, 1968) interpolation
Climatology	IAP climatology: simple gridded average and then spatial interpolation with distance-weighted average	Improved IAP reconstruction with EnOI approach
XBT bias correction	CH14 (updated in 2018)	CH14 (revised and updated in 2023)
MBT bias correction	IK09 (Ishii and Kimoto, 2009)	GC20 (Gouretski and Cheng, 2020)
APB bias correction	None	GCR24 (Gouretski et al., 2024)
Bottle bias correction	None	GCT22 (Gouretski et al., 2022)
Mapping	EnOI-DE with influencing radius of 20, 8, 3 degrees, iteratively.	EnOI-DE with influencing radius of 2000, 800, 300 km, iteratively. Representative error updated with 2005–2022 observations. The radius of influence does not cross the land.
Uncertainty	Given by EnOI framework accounting for instrumental error and horizontal sampling/mapping error	Given by EnOI framework accounting for instrumental error and horizontal sampling/mapping error
DOI	/	http://dx.doi.org/10.12157/IOCAS.20240117.002 for temperature data (Cheng et al., 2024a) and http://dx.doi.org/10.12157/IOCAS.20240117.001 for ocean heat content data (Cheng et al., 2024b)

406 2.7 OHC calculation and volume correction

407 Based on the gridded temperature reconstruction (Table 1), OHC in each grid is
408 calculated as $OHC(x, y, z) = c_p \iiint_{V(x,y,z)} \rho T dV(x, y, z)$. following TEOS-10 standards,
409 where c_p is a constant of $\sim 3991.9 \text{ J (kg K)}^{-1}$ according to the new TEOS-10 standard
410 formulation as conservative temperature and absolute salinity are used, ρ is potential
411 density in kg m^{-3} , and T is conservative temperature measured in degrees Celsius (here it
412 is anomaly relative to the 2006–2020 baseline) (Cheng et al., 2022a).

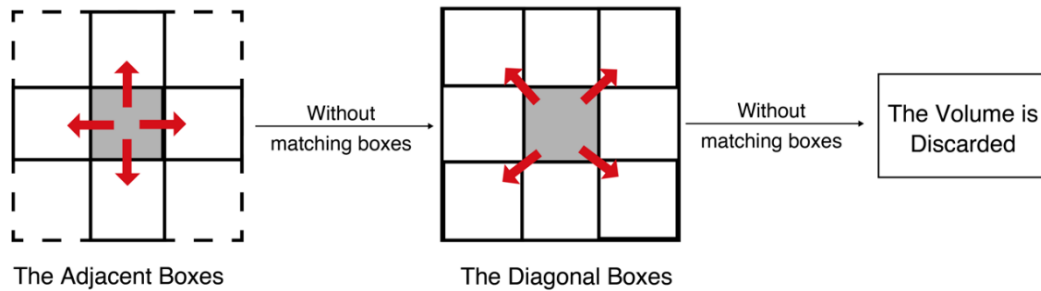
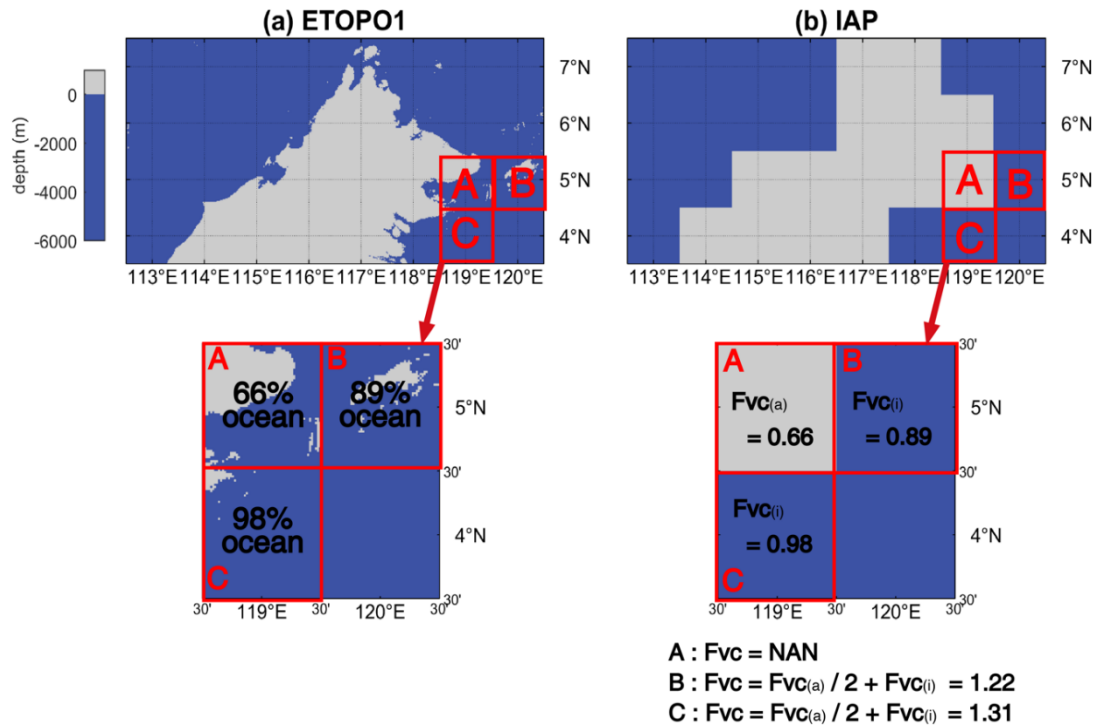
413 As OHC is an integrated metric over a specific ocean volume, properly identifying
414 ocean volume is critical, especially in shallow waters. Previous studies found a 10–20 %
415 difference in the OHC trend in recent decades between different land-ocean masks (von
416 Schuckmann and Le Traon, 2011; Meyssignac et al., 2019; Savita et al., 2022).
417 Specifically, in marginal sea areas with complex topography, $1^\circ \times 1^\circ \times \Delta z$ grid boxes
418 (where Δz is the depth range of the grid box) near coasts and islands typically cover both
419 ocean and land areas but are assigned to represent land or ocean only. Thus, the gridded
420 ocean temperature datasets are subjected to errors from inaccurate land-sea attribution.
421 Here, we offer a volume correction (VC) for these grid boxes to improve the OHC
422 estimate, as follows.

423 For each $1^\circ \times 1^\circ \times \Delta z$ grid box, we introduce a VC factor (denoted as F_{VC}) to correct
424 the OHC values: $OHC_{VC}(x, y, z) = OHC(x, y, z) \times F_{VC}(x, y, z)$. First, we assume the
425 seawater volume distribution in 1 arc-minute topographic data of ETOPO1 as “truth”. No
426 correction is needed if a box is assigned to ocean according to ETOPO1 data, thus, $F_{VC}=1$.
427 If a fraction of a $1^\circ \times 1^\circ \times \Delta z$ grid box is land according to ETOPO1 and IAP data includes
428 T/OHC values, the F_{VC} is represented by the fraction of the ocean volume in this box
429 (illustrated in Fig. 5), and the volume for OHC calculations can be corrected with $F_{VC}(i)$. In
430 a grid box, if there is no IAP data (i.e., it is land according to the IAP mask), but this box
431 contains some ocean volume according to ETOPO1 data, we define $F_{VC}(a)$ again as the
432 fraction of the ocean volume in this box, and then this $F_{VC}(a)$ is added to the adjacent grid
433 boxes where there are values in IAP data. If all the adjacent grid boxes contain no data, the
434 volume is equally redistributed to the diagonal boxes (Fig. 5). The volume is discarded if
435 there is no data in all adjacent and diagonal boxes.

436 With this approach, the VC factor in each grid box is a sum of two components: a
437 local adjustment $F_{VC}(i)$ and a redistribution from the adjacent grids:

438 $F_{VC}(a)$: $F_{VC} = F_{VC}(i) + F_{VC}(a)$,

439 To avoid misidentification of sea ice, we performed VC only on the global grid points
440 within 60 °S to 60 °N. Eventually, we obtained a three-dimensional FVC that fits the IAP
441 grids (119 × 360 × 180; depth coverage to 6000 m) and used it to compute OHC. The VC
442 applied to ~15% of all the $1^\circ \times 1^\circ \times \Delta z$ grid boxes of IAPv4 ocean grid boxes (with $F_{VC} \neq$
443 1) for the entire 0-6000 m ocean and ~10% grid boxes of the upper 2000 m. Since the open
444 ocean accounts for the vast majority of the global ocean volume, the influence of the VC
445 method on the global OHC trend is small. For example, the upper 2000 m OHC trend with
446 VC is ~0.15% (~0.45%) smaller than without VC from 1958-2023 (2005-2023) for IAPv4.
447 However, it can significantly affect regional OHC estimates, especially in regions with
448 complex topography. For example, the Maritime Continent region's 0-2000 m OHC trend
449 is reduced by 6.9% (4.2%) after applying VC from 1958-2023 (2005-2023) (Jin et al.,
450 2024).



451

452 **Figure 5:** An example explaining the Volume Correction algorithm. (a) Bathymetry
453 derived from ETOPO1. (b) Bathymetry in IAPv4 analysis.

454

455 2.8 Independent datasets for comparison and evaluation

456 Four Sea Surface Temperature (SST) datasets are used to evaluate the upper-most
457 layer (1 m) of IAPv4, including Extended Reconstructed SST version 5 (ERSST5) (Huang
458 et al., 2017); Japan Meteorological Agency Centennial Observation-Based Estimates of
459 SSTs version 1 (COBE1) (Ishii et al., 2005), and its version 2: COBE2 (Hirahara et al.,
460 2014); Hadley Centre Sea Ice and Sea Surface Temperature dataset (HadISST) (Rayner et
461 al., 2003). The anomalies relative to a 2006-2020 average were computed by removing the
462 monthly climatology. Measurements of SST are made *in situ* by means of thermometers or
463 retrieved remotely from infrared and passive microwave radiometers on satellites
464 (Kennedy, 2014; O'Carroll et al., 2019). Satellite SST observations began in the early

465 1980s. *In situ* SST observations go back to the 19th century and involve many different
466 measurement methods, including wooden and later insulated metal buckets to collect water
467 samples, engine room inlet measurements, and sensors on moored and drifting buoys
468 (Kennedy, 2014). The subsurface temperatures are collected as “profiles” which contain
469 multiple measurements at discrete vertical levels. Because of the differences in observation
470 systems, SSTs are fundamentally different in their temporal and spatial coverage and
471 temporal extent compared to subsurface observations on which OHC estimates rely. SST
472 measurements also have different uncertainty sources and error structures; thus, the two
473 systems are typically treated as independent data sources and have been used for cross-
474 validation (Gouretski et al., 2012).

475 An independent *in situ* observation dataset in the Labrador Sea is used to evaluate
476 IAPv4. This dataset, provided by the Bedford Institute of Oceanography (BIO)
477 (Yashayaev, 2007; Yashayaev and Loder, 2017), includes independently validated and
478 bias-corrected data from multi-section hydrological surveys (i.e., AR7W) in the Labrador
479 Sea, spanning from 1896 to 2020 (this study used 1960-2020 data). These data have not
480 been incorporated into the WOD.

481 The capability of the new product to close the sea level budget and the Earth’s energy
482 budget also provides tools for validation. A superior dataset should be capable of closing
483 the sea level and the Earth’s energy budgets. The total sea level change has been monitored
484 via satellite altimetry since 1993 (from the University of Colorado
485 <https://sealevel.colorado.edu/>). The ocean mass change is derived from JPL RL06.1Mv3
486 Mascon Solution GRACE and GRACE-FO data since 2002 (Watkins et al., 2015). For
487 long-term total sea level change since the 1950s, we use a tide-gauge-based reconstruction
488 (Frederikse et al., 2020). During the same period, the estimates of the Greenland ice sheet,
489 Antarctic ice sheet, land water storage, and glacier ice melt contributions from Frederikse
490 et al., (2020) are used to derive ocean mass change. To derive steric sea level, IAP salinity
491 data is used (Cheng et al. 2020). The temperature and salinity data are converted to steric
492 sea level based on the Thermodynamic Equation Of Seawater – 2010 (TEOS-10) standard
493 (McDougall and Barker, 2011).

494 For the energy budget, the ice, land, and atmosphere heat content changes are from
495 (von Schuckmann et al., 2023) from 1960 to the present. Because of the less reliable data
496 before the 1990s for land, sea ice and ice sheets, the other set of land–atmosphere–ice data
497 from 2005–19 is used as in Trenberth, (2022) to investigate the recent changes. The net

498 radiation change at the top of the atmosphere is based on Clouds and Earth's Radiant
499 Energy Systems (CERES) Energy Balanced and Filled (EBAF) data from Loeb et al.,
500 (2021) and Loeb et al., (2018) and Deep-C data from the University of Reading (Liu and
501 Allan, 2022; Liu et al., 2017).

502 Several gridded ocean T/OHC gridded products are used here for inter-comparison,
503 including the IAPv3 (Cheng et al., 2017), the EN4 ocean objective analysis product from
504 the UK Met Office Hadley Centre (Good et al., 2013); the ocean objective analysis product
505 (Ishii et al., 2017) (termed “ISH” hereafter) from JMA, an Argo-only gridded product from
506 SCRIPPS (Roemmich and Gilson, 2009) (termed “RG” hereafter), and an OHC product
507 based on random forest regressions (termed “RFROM” hereafter) using in situ training
508 data from Argo and other sources on a 7-day \times 1/4° \times 1/4° grid with latitude, longitude,
509 time, SSH, and SST as predictors (Lyman and Johnson, 2023). Several datasets available
510 in IPCC-AR6 (Gulev et al., 2023) are used for comparison, including: the PMEL product
511 from Lyman and Johnson, (2014); Machine learning based reconstruction of OHC by
512 Bagnell and DeVries, (2021); BOA product based on refined Barnes successive corrections
513 by the China Argo Real-time Data Center (Li et al., 2017); International Pacific Research
514 Center (IPRC) (2005-2020), von Schuckmann and Le Traon 2011 (KvS11); Green function
515 based OHC estimate derived from SST (Zanna et al., 2019).

516

517 **2.9 Trend calculation and uncertainty estimates**

518 The trends in this study have been estimated by a LOWESS approach (Cheng et al.,
519 2022b), i.e., we apply a locally weighted scatterplot smoothing (LOWESS) to the time
520 series (25-year window, equal to an effective 15-years smoothing), and then the OHC
521 difference between the first and the end year is used to calculate the trend. This approach
522 provides an effective method to quantify the local trend by minimizing the impact of year-
523 to-year variability and start/end points.

524 Throughout this paper, the 90 % confidence interval is shown. The uncertainty of
525 trend also follows the approach in Cheng et al., (2022a) based on a Monte Carlo
526 simulation. First, a surrogate OHC series is formed by simulating a new residual series
527 (after removing the LOWESS smoothed time series) based on the AR(1) process and
528 adding it to the LOWESS line. Then a LOWESS trendline is estimated for each surrogate.
529 This process is repeated 1000 times, and 1000 trendlines are available. The 90 %
530 confidence interval for the trendline is calculated based on ± 1.65 times the standard

531 deviation of all 1000 trendlines of the surrogates. Secondly, the uncertainty in the rate of
532 the OHC is estimated by the 1000 LOWESS trendlines: 1) calculating the rate based on the
533 difference between the first and last annual mean value of the LOWESS trendline in a
534 specific period; 2) calculating ± 1.65 times the standard deviation of the 1000 rate values.

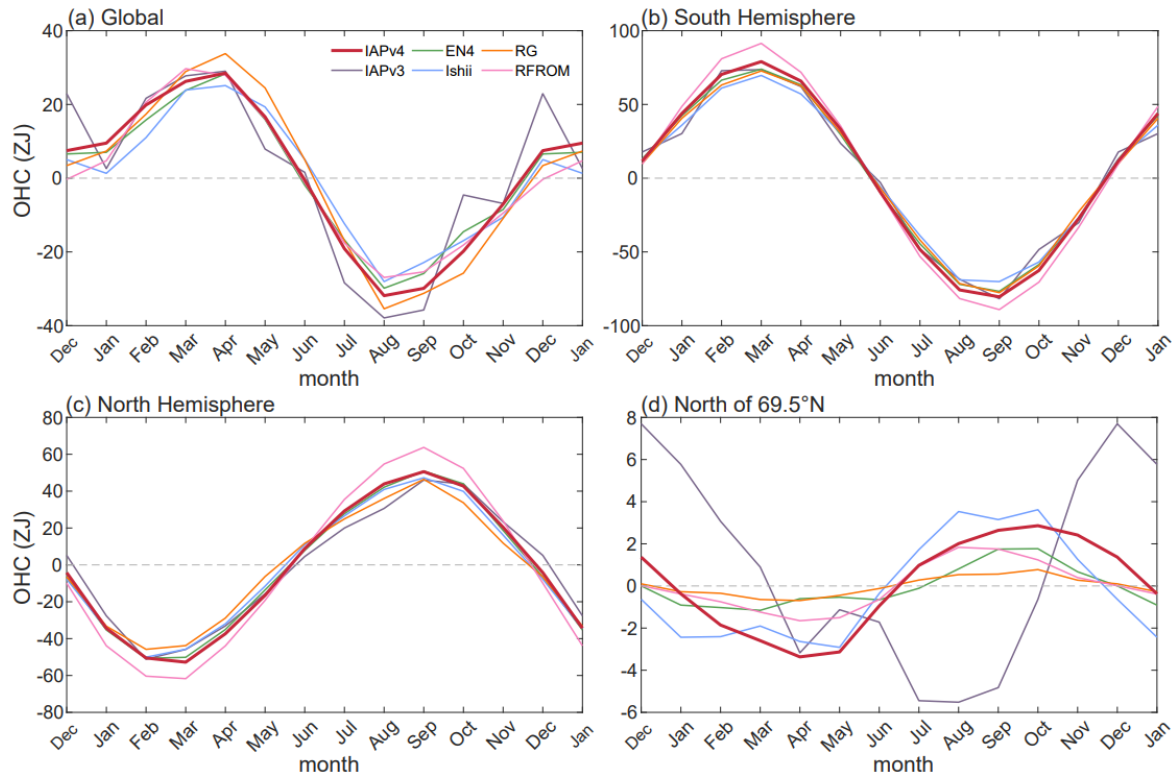
535

536 **3. Results**

537 **3.1 Climatological annual cycle**

538 The annual cycle of the OHC above 2000 m of IAPv4 is compared with IAPv3, ISH,
539 EN4, RG and RFROM (Fig. 6 and Fig. 7) for 2006–2020. There is a consistent annual
540 cycle among different datasets for the global and hemispheric oceans. Globally, the ocean
541 releases heat from boreal spring to autumn and accumulates heat from boreal autumn to
542 spring, which is dominated by the southern hemisphere due to its larger ocean surface area
543 (Fig. 6). The two hemispheres show opposite annual variations in OHC, associated with
544 the annual change of solar radiation and different distribution of land and sea. For the
545 global OHC above 2000 m, IAPv4 shows a positive peak in April and a dip in August,
546 with the magnitude of OHC variation of 60.4 ZJ for IAPv4 (66.9 ZJ for IAPv3), consistent
547 with other datasets: 53.2 ZJ for ISH, 58.1 ZJ for EN4, 69.2 ZJ for RG and 56.6 ZJ for
548 RFROM (where 1 ZJ = 10^{21} J).

549 There are some unphysical variations in the OHC annual variations for IAPv3 (blue
550 lines). For example, the global OHC shows large spikes in January and December, and a
551 big shift from September to October, by contrast, the other three data products show much
552 smoother changes (Fig. 6a). The IAPv3 Arctic OHC (north of 69.5 °N) shows different
553 phase change compared with the other datasets together with a big shift from September to
554 December, and the magnitude of variability is much larger in IAPv3 than other datasets
555 (Fig. 6d). The improvement in IAPv4 is mainly because of the methodology
556 improvements: IAPv3 used 1990–2005 data to construct climatology which suffered from
557 errors related to sparse data coverage, use of “degree distance” instead of “km distance”,
558 and other error sources. Therefore, the IAPv4 analysis presents a physically tenable OHC
559 seasonal variation.



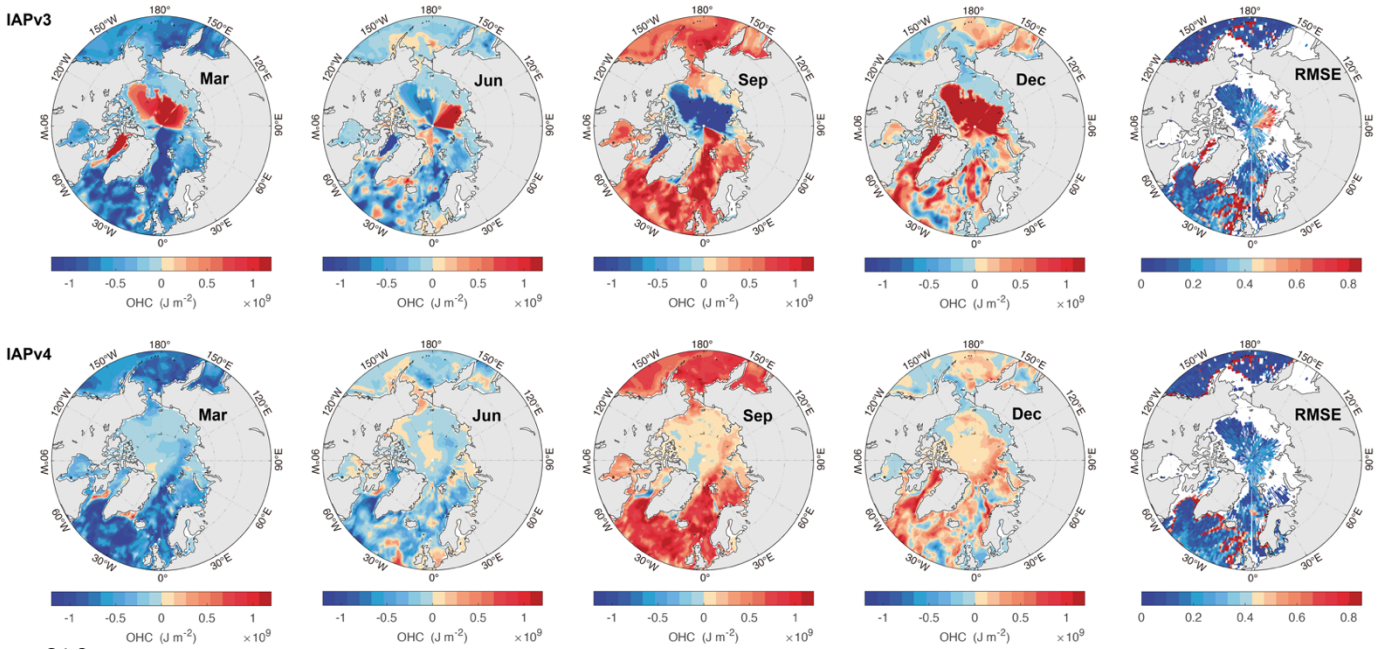
560

561

562 **Figure 6: Annual cycle of OHC of upper 2000 m for (a) the global oceans, (b) the**
 563 **Southern Hemisphere, (c) the Northern Hemisphere and (d) the oceans north of**
 564 **69.5°N. Five different data products are presented, including IAPv4 (red), IAPv3 (black),**
 565 **ISH (purple), EN4 (green), RG (orange), and RFROM (pink).**

566

567 IAPv4 OHC data shows significant improvements in the Arctic region, reflected in
 568 both the spatial distribution and seasonal variation of OHC. In IAPv3, the maximum upper
 569 2000 m OHC occurs in December, and the minimum OHC occurs in August. However, for
 570 IAPv4, the maximum amounts to 2.9 ZJ in October and decreases to a minimum of -3.4 ZJ
 571 in April. This estimate of the Arctic annual cycle is consistent with a constrained Arctic
 572 OHC estimate with atmospheric data by enforcing energy budget closure (Mayer et al.,
 573 2019). Furthermore, the spread of the OHC annual cycle in the Arctic region across
 574 different datasets is reduced from 5.2 ZJ to 2.5 ZJ, indicating a smaller uncertainty. The
 575 spatial OHC anomaly distribution in the Arctic region of the IAPv4 is more spatially
 576 homogeneous than IAPv3, and IAPv3 appears as rays emerging from the pole which are
 577 not physical (Fig. 7). IAPv4 displays a consistent seasonal variation north of 69.5 °N
 578 mainly because of the changes of the influencing radius from “degrees” to “kilometers”.



580 **Figure 7: Seasonal distribution of monthly mean upper 2000 m OHC anomalies**
 581 **and root mean square error (RMSE) of OHC 0-2000 m between gridded data and in**
 582 **situ observations. For OHC anomalies, four months are shown: March, June,**
 583 **September, and December. The OHC anomalies are relative to the 2006 – 2020**
 584 **annual mean.** The upper and lower panels are for IAPv3 and IAPv4 products,
 585 respectively. The panels in the last column are for annual RMSE for IAPv3 (upper) and
 586 IAPv4 (lower), respectively.

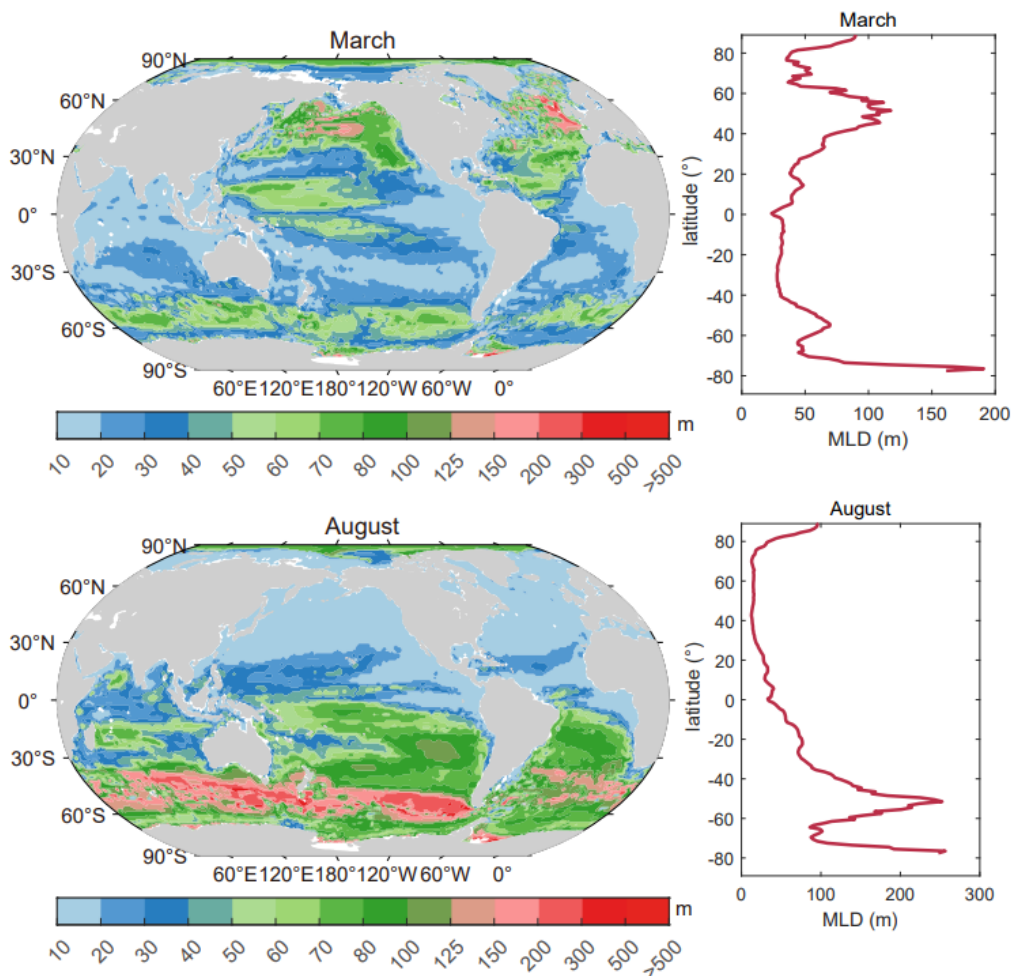
587

588 3.2 Mixed layer depth

589 Mixed layer depth (MLD) provides a crucial parameter of upper ocean dynamics
 590 relevant for upper-deeper ocean and air-sea interactions. Spatial distributions of the MLD
 591 in March and August are shown in Fig. 8 for IAPv4, based on criteria of $\Delta T = 0.2 \text{ }^\circ\text{C}$
 592 temperature for the 10 m depth temperature. As expected, the seasonal variations of the
 593 MLD are generally opposite in the northern and southern hemispheres. The MLD shows a
 594 much stronger seasonal variation in the subtropics and midlatitudes (for example, $20^\circ\sim 70^\circ$
 595 in both hemispheres) than in other regions (including the tropics, for example,
 596 $20^\circ\text{S}\sim 20^\circ\text{N}$), which is manifested as shallower MLD ($\sim 20 \text{ m}$) in summer due to strong
 597 surface heating that increases stratification, and deeper MLD ($>70 \text{ m}$) because of
 598 surface cooling and increased surface wind creating stronger mixing.

599 In the north hemisphere, the maximum MLD occurs during the wintertime in the
 600 subpolar North Atlantic deep water formation regions ($40^\circ\text{N} \sim 65^\circ\text{N}$), with values over

601 500 m in the Iceland Basin. In comparison, in the midlatitudes, the maximum of MLD is
 602 generally less than 125 m in the wintertime. The MLD minimum in the north hemisphere is
 603 in the summertime, and the values are mostly within 20 m depth. In the Southern
 604 Hemisphere, the MLD maximum values (deeper than 300 m) occur between 45 °S and
 605 60 °S of the Southern Ocean (north of the Antarctic Circumpolar Current) in the boreal
 606 summer where the year-round intense westerly winds are located. The minimum MLD in
 607 this region in the boreal winter is less than 70 m. The seasonal variation of the MLD is
 608 well established by previous studies (Chu and Fan, 2023; de Boyer Montégut et al., 2004;
 609 Holte et al., 2017), and this evaluation confirms that IAPv4 temperature data is capable of
 610 reasonably representing the MLD. However, as pointed out by de Boyer Montégut (2004),
 611 the MLD estimated from the average temperature profiles might lead to an underestimation
 612 of MLD by ~25% compared to the MLD computed from individual profiles based on the
 613 same 0.2 °C criterion method. This potential issue needs further investigation.



614

615 **Figure 8: Spatial pattern of the climatological mean MLD (left panels) and zonal**
 616 **mean MLD (right panels) in March (top) and August (bottom) estimated from the**

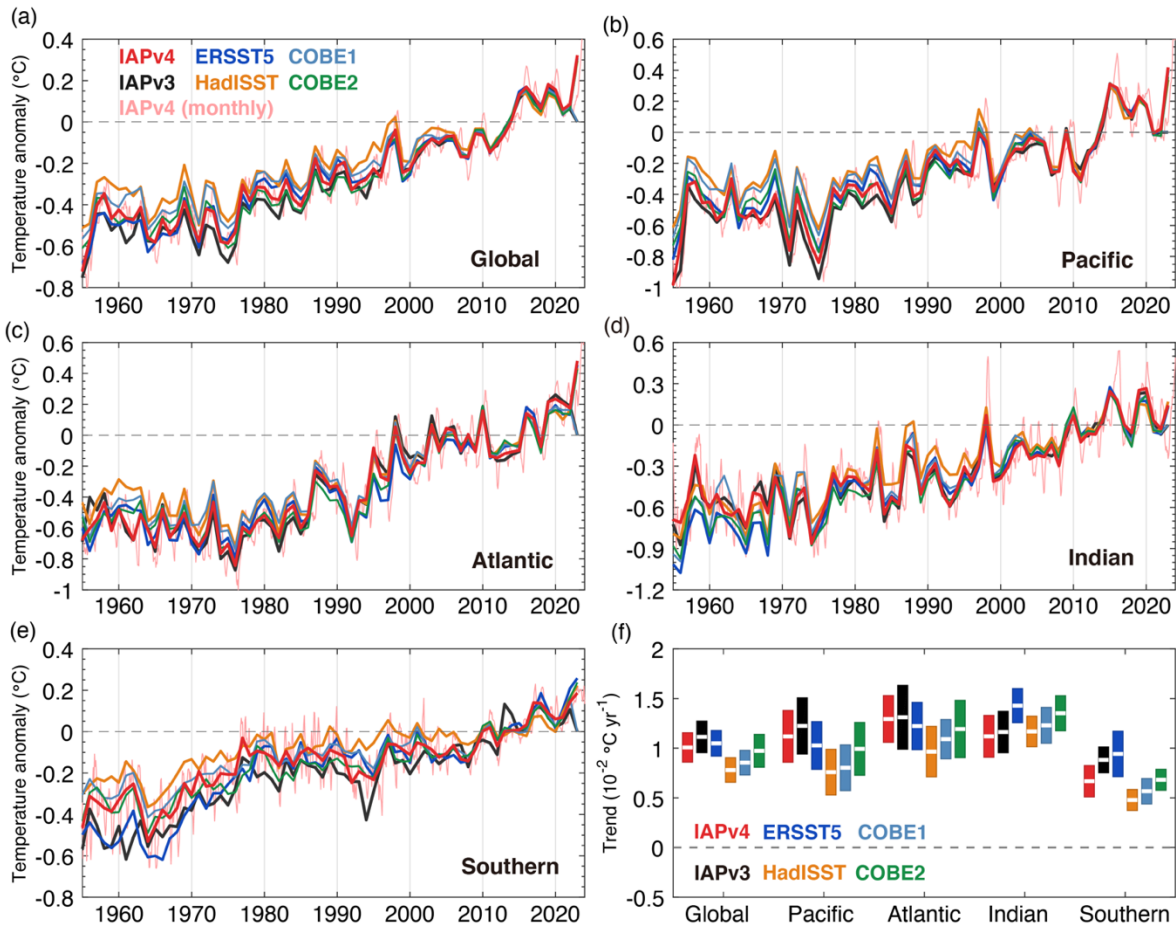
617 **IAPv4.** Here, the MLD is calculated using the temperature difference criterion of $\Delta T =$
618 $0.2\text{ }^{\circ}\text{C}$ between the surface and 10-meter depth.

619

620 **3.3 Sea surface temperature**

621 IAPv4 and IAPv3 temperature time series at 1 m depth (Fig. 9) are compared with
622 four independent SST data products (ERSST5, HadISST, COBE1, and COBE2). All data
623 products including IAPv4 show robust sea surface warming in the global ocean and four
624 main basins since 1955 (Fig. 9). Since the HadISST and COBE2 data did not include the
625 year 2023, we compare the long-term SST trend during 1955–2022 using these products
626 (Fig. 9f). The global-mean IAPv4 SST rate between 1955 and 2022 is $1.01 \pm 0.15\text{ }^{\circ}\text{C}$
627 century^{-1} (90 % CI), which is within the range of the SST products (ranging from 0.78 to
628 $1.05\text{ }^{\circ}\text{C century}^{-1}$). The 1955–2022 trend of IAPv4 SST is slightly weaker than IAPv3 for
629 the global ocean ($1.11 \pm 0.16\text{ }^{\circ}\text{C century}^{-1}$) and all the ocean basins. The largest difference
630 between IAPv4 and other SST products comes mainly from the Pacific and the Southern
631 Ocean before 1980, associated with sparser in situ observations for both SST and
632 subsurface temperature data.

633 The spatial distribution of long-term SST trends over the 1955–2022 period provides
634 insights into the data consistencies and differences. First, IAPv4 shows a pattern of SST
635 consistent with other datasets (Fig. 10). More rapid warming is found in the poleward
636 western boundary currents regions, such as the East Australian Current and the Gulf
637 Stream. The warmer ocean in the upwelling areas, such as the Tropical Eastern Pacific and
638 Gulf of Guinea, are identified by all data products. The surface warming in the South
639 Indian for IAPv4 data is weaker than for IAPv3, ERSST5, and COBE2 but is more
640 consistent with HadISST and COBE1. The surface cooling to the south of $60\text{ }^{\circ}\text{S}$ can also
641 be found in all the datasets but with some discrepancies in magnitude and locations related
642 to data sparsity. The tropical Pacific SST trends are mostly insignificant in the eastern and
643 south-eastern Pacific Ocean because of the strong inter-annual and decadal fluctuations
644 (Figure not shown).



645

646

647

648

649

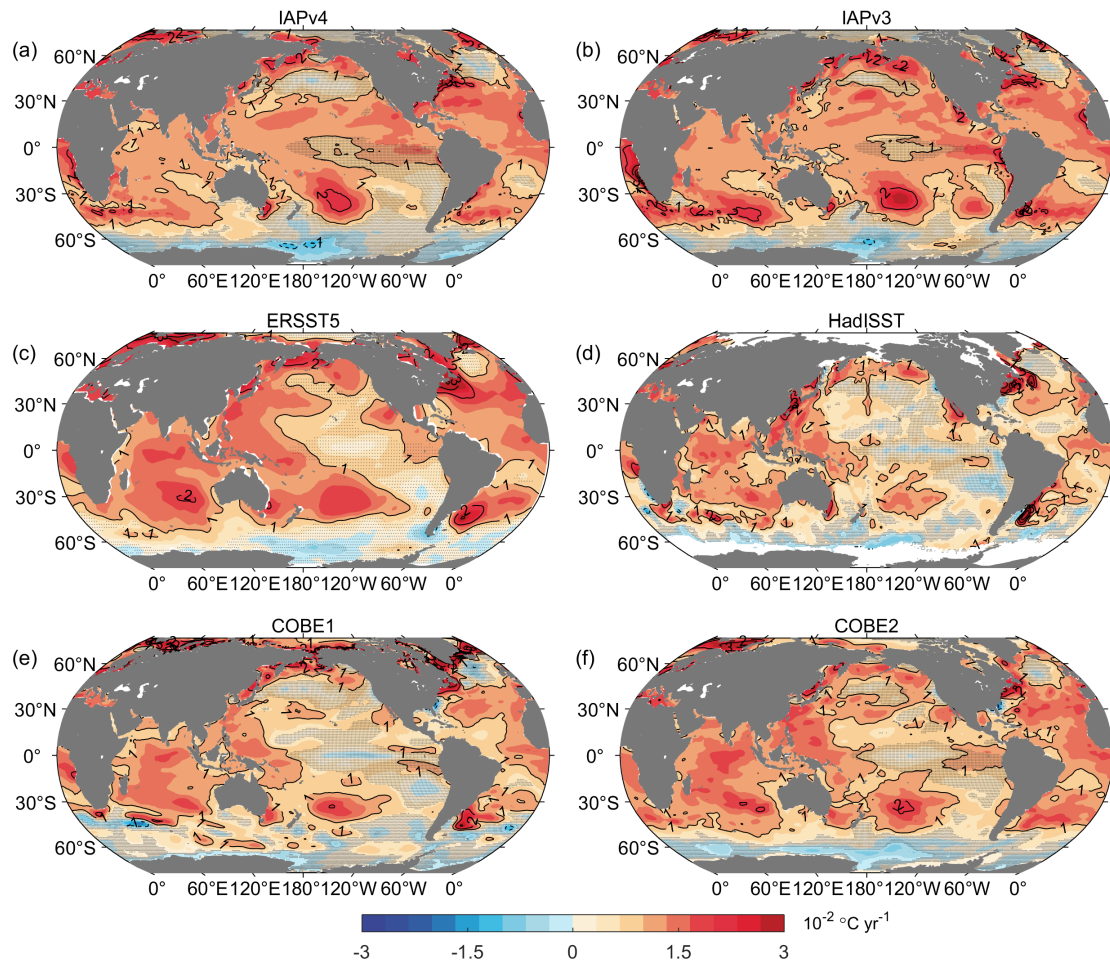
650

651

652

653

Figure 9: Global and basin time series of SST change for IAPv4, compared with ERSST/HadISST/COBE1/COBE2 and IAPv3 from 1955 to present. (a) Global, (b) Pacific, (c) Atlantic, (d) Indian and (e) Southern oceans (South of 30 °S) (units: °C). (f) shows the warming rate from 1955 to 2022. The pink thin line is the monthly time series of IAPv4 SST and other time series are annual time series of different datasets. The vertical scales are different for different panels. All anomaly time series are relative to a 2006–2020 baseline.



654

655 **Figure 10: Spatial maps of the SST long-term trends during the 1955–2022 period.** (a)
 656 IAPv4, (b) IAPv3, (c) ERSST5, (d) HadISST, (e) COBE1 and (f) COBE2 (units: $10^{-2} \text{ }^\circ\text{C}$
 657 yr^{-1}). The contour line interval is $0.5 \times 10^{-2} \text{ }^\circ\text{C yr}^{-1}$. The stippling indicates the regions with
 658 signals that are not statistically significant (90 % CI).

659

660 3.4 Global OHC time series

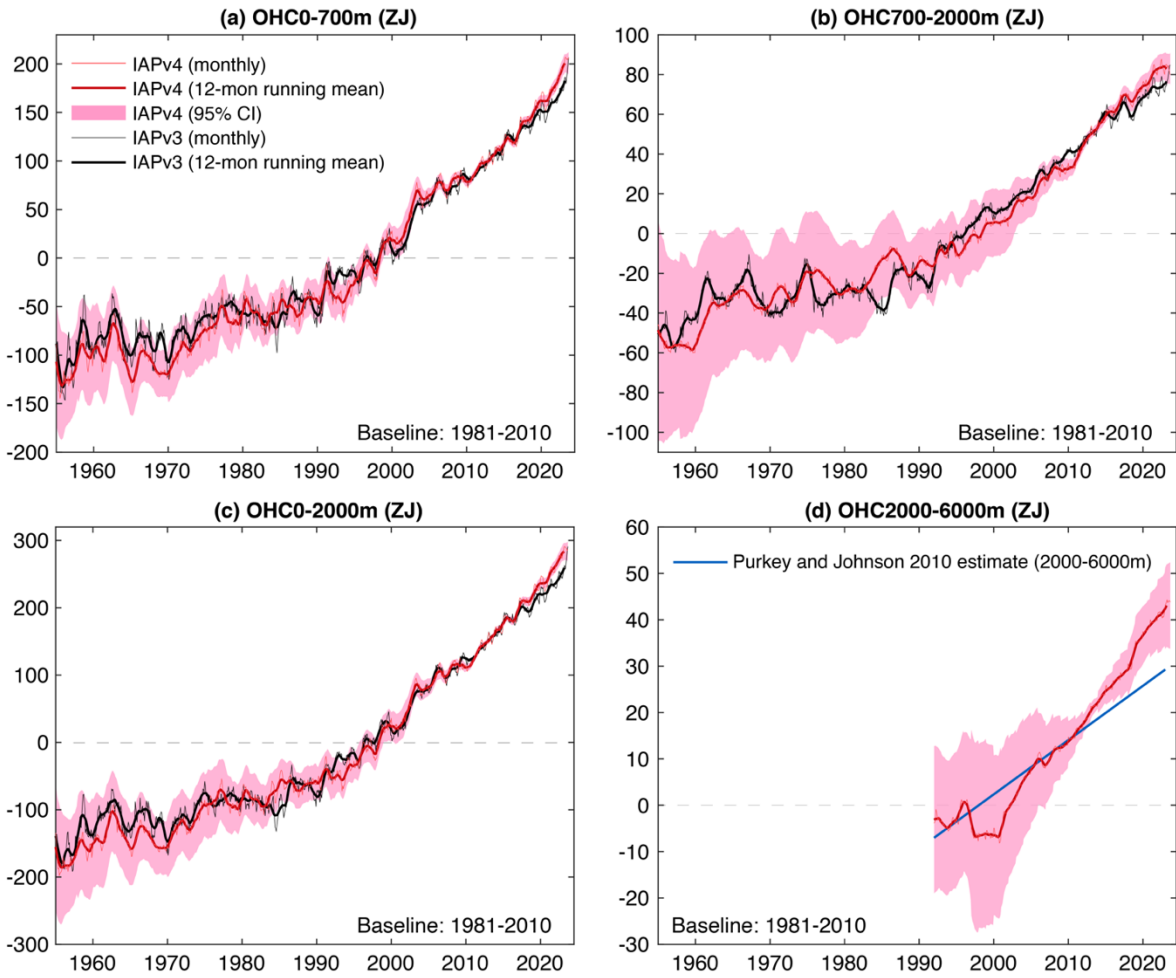
661 Global OHC time series for 0–700 m, 700–2000 m, 0–2000 m, and 2000–6000 m
 662 layers of IAPv4 (Fig. 11) for 1955–2023 versus IAPv3 show a robust ocean warming, with
 663 a linear warming rate of $4.4 \pm 0.2 \text{ ZJ yr}^{-1}$ (0–700 m), $2.0 \pm 0.1 \text{ ZJ yr}^{-1}$ (700–2000 m), and
 664 $6.4 \pm 0.3 \text{ ZJ yr}^{-1}$ (0–2000 m). The long-term warming revealed by IAPv4 is greater than
 665 IAPv3 ($4.1 \pm 0.2 \text{ ZJ yr}^{-1}$ for 0–700 m, $1.9 \pm 0.1 \text{ ZJ yr}^{-1}$ for 700–2000 m and 6.0 ± 0.3
 666 ZJ yr^{-1} for 0–2000 m). Before ~1980, bottle bias correction reduces the time-varying
 667 systematic warm bias in Nansen bottle data and leads to a stronger warming rate from
 668 1955–1990. The updated MBT and XBT corrections are mainly responsible for the

669 difference between 1980 and 2000 (Cheng et al., 2014; Gouretski and Cheng, 2020). Data
670 QC impacts the intra-seasonal and inter-annual variation of the OHC time series (Tan et
671 al., 2023). Also, because of the application of Bottle/XBT/MBT corrections, IAPv4 shows
672 a stronger upper 2000 m ocean warming trend than most of the other available products
673 assessed in Fig. 12.

674 From 2005–2023, the new IAPv4 product shows stronger warming than IAPv3. The
675 mean upper 2000 m warming rate is 10.7 ± 1.0 ZJ yr⁻¹ for IAPv4 and 9.6 ± 1.1 ZJ yr⁻¹ for
676 IAPv3 (Fig. 11), mainly because of the replacement of the WOD-QC system by the new
677 CODC-QC system in IAPv4. Tan et al., (2023) indicated that the WOD-QC system had
678 removed more extreme higher temperature values in the regions of warm eddies and
679 marine heat waves than CODC-QC. The IAPv3 700–2000 m OHC shows a much bigger
680 drop in 2018 than IAPv4 (Fig. 11b), while the IAPv4 indicates an approximately linear
681 700–2000 m warming since 2005, resulting in stronger 700–2000 m warming in IAPv4
682 (3.6 ± 0.5 ZJ yr⁻¹) than in IAPv3 (2.9 ± 0.5 ZJ yr⁻¹). Compared with other available
683 products shown in Fig. 12, IAPv4 shows a similar OHC 0–2000 m trend to RFROM from
684 2005–2023, but with stronger warming trends than the two Argo-based products (BOA and
685 SCRIPPS). From 1993–2023, IAPv4 showed a stronger OHC 0–2000 m trend than NCEI,
686 Ishii, OPEN, and Zanna data and a slightly weaker trend than PMEL and RFROM (Fig.
687 12).

688 Since the 1990s, the World Ocean Circulation Experiment (WOCE) provided a global
689 network of abyssal ocean observations, sustained by repeated hydrological lines and a
690 deep-Argo program (Katsumata et al., 2022; Roemmich et al., 2019; Sloyan et al., 2019).
691 These high-quality data provide an opportunity to estimate deep OHC changes below 2000
692 m in this study. IAPv4 provides a new OHC estimate below 2000 m by collecting 5 years
693 of data centered on each month. The result (Fig. 11d) indicates a robust abyssal (2000–
694 6000 m) ocean warming trend since ~1993 of 2.0 ± 0.3 ZJ yr⁻¹. This is higher (within the
695 uncertainty range) than the previous estimate of 1.17 ± 0.5 ZJ yr⁻¹ in Purkey and Johnson
696 (2010) but consistent with the recent assessment showing the acceleration of deep ocean
697 warming in the Southwest Pacific Ocean (Johnson et al., 2019).

698



699

700 **Figure 11: Global OHC time series for 0–700 m (a), 700–2000 m (b), 0–2000 m (c) and**

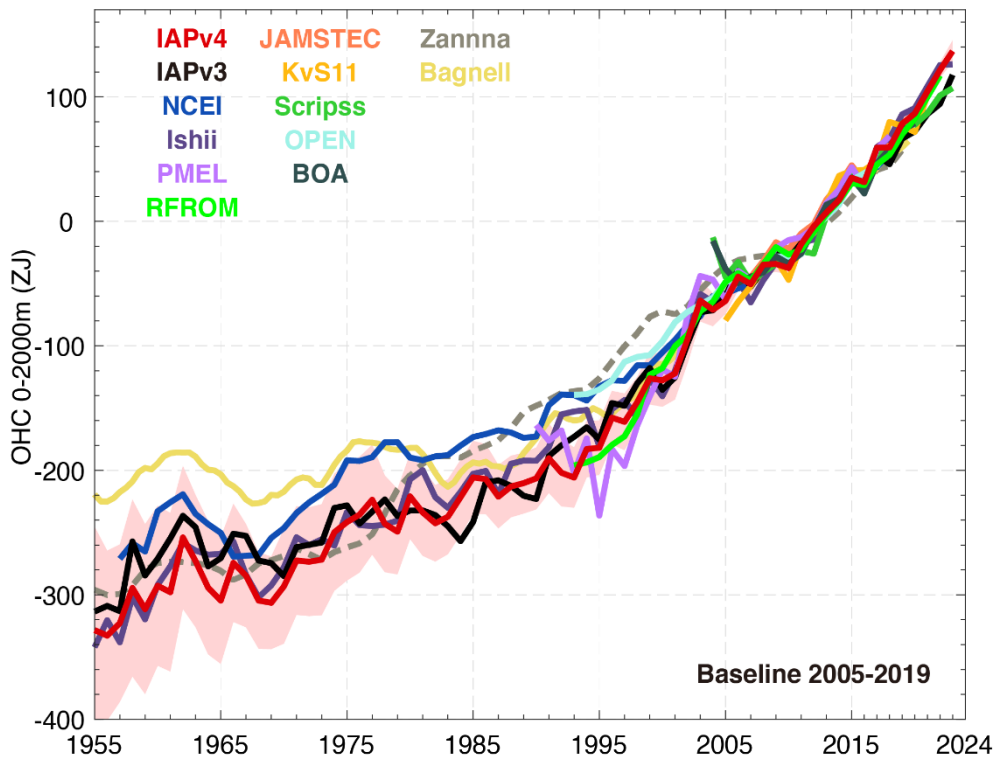
701 **2000–6000 m (d). All-time series are relative to a 1981–2010 baseline. The shading**

702 **indicates the 90 % confidence interval. The vertical scales are different for different panels.**

703

The unit is ZJ.

704



705

706

707

708

709

710

711

712

713

714

715

716

717

718

719

720

721

722

723

724

Figure 12: A comparison of annual mean OHC 0-2000 m time series from different data products. Solid and dashed lines represent direct and indirect estimates, respectively, and shading indicates the IAPv4 90% confidence interval (pink shading). OHC anomalies are relative to a 2005–2019 baseline. The plot is updated from Cheng et al. (2022a).

Another feature of IAPv4 is the suppression of month-to-month noise compared to many available data products. Trenberth et al. (2016) noted that the month-to-month variation (quantified by the standard deviation of the monthly $dOHC/dt$ time series) in all *in situ*-based OHC records is much larger than implied by the CERES records, suggesting that the OHC variation on this time scale is most likely spurious. Therefore, the magnitude of the month-to-month variation in the OHC record can be used as a benchmark of the data quality. The standard deviation of the CERES record is 0.67 Wm^{-2} from 2005 to 2023 (Loeb et al., 2018). While IAPv4, IAPv3, ISH, EN4, BOA, NCEI, and SIO data show a standard deviation of $dOHC/dt$ time series of 3.52, 3.52, 7.49, 8.79, 10.05, 11.29, 10.00 Wm^{-2} , respectively for the upper 2000 m (Table 2). Note that differentiation to get the rate of change amplifies noise, and applying a 12-month running smoother significantly knocks down the noise so that the IAPv4 standard deviation becomes 0.75 Wm^{-2} , the smallest among the datasets investigated in this study (Table 2) and is the most physically plausible time series from this noise-level perspective. In addition, Lyman and Johnson's (2013) data

725 suggest a yearly variance ratio of 1.3 between annual RFROM and CERES data from 2008
 726 to 2021. Using the yearly mean OHCT indicates a ratio of 1.4 at the same period between
 727 IAPv4 and CERES, which is similar to that of RFROM.

728

729 **Table 2. Characteristics of Month-to-month variation of OHCT compared with**
 730 **CERES.** Comparisons of different ocean gridded products: the monthly standard deviation
 731 (std dev) of the monthly rates of change of OHC (W m^{-2}); the corresponding standard
 732 deviation of the 12-month running mean (13-points are used, with start-point and endpoint
 733 weighted by 0.5), and the linear trend with 90% confidence limits (Wm^{-2}) (global surface
 734 area). The values are for 2005–2022. The OHC trend for CERES is calculated as the mean
 735 of net TOA radiation flux within 2005–2022 multiplied by 0.9, assuming 90% of the EEI
 736 stored in the ocean.

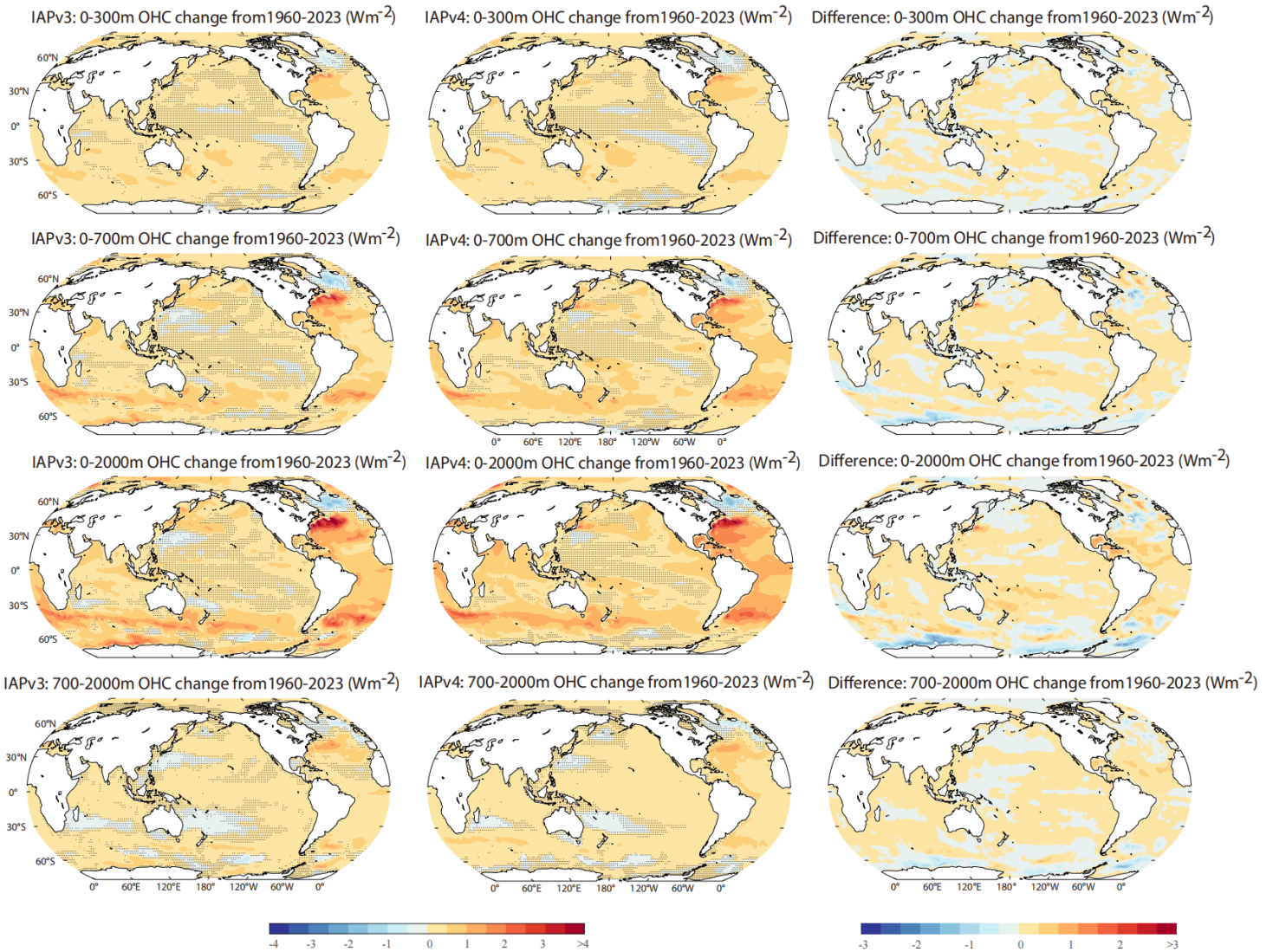
Source	Std dev	Std dev (12 month)	OHC Trend (2005–2022)
IAPv4	3.52	0.75	0.66 ± 0.04
IAPv3	3.52	0.79	0.56 ± 0.03
ISH	7.49	1.35	0.63 ± 0.05
EN4	8.79	1.03	0.67 ± 0.04
BOA	10.05	1.16	0.60 ± 0.07
NECI	11.29	1.11	0.61 ± 0.07
SIO	10.00	1.24	0.56 ± 0.08
CERES	0.67	0.33	0.77

737

738 3.5 Regional OHC trends

739 For 1960–2023 (Fig. 13), the IAPv4 trends are slightly weaker than IAPv3 in the
 740 Pacific Ocean but slightly higher in the Atlantic Ocean (Fig. 13), with more than 95 % of
 741 the ocean area showing a warming trend. The polar regions also show remarkable
 742 differences compared to IAPv3 (Section 3.1), mainly because of the change of covariance,
 743 which improves the spatial reconstruction in the polar regions. The IAPv4 shows stronger
 744 warming near the boundary currents regions, mainly because of the improved QC that does
 745 not flag high-temperature anomalies. Nevertheless, the pattern of trends is very similar in
 746 the two versions of data, indicating the robustness of the ocean warming pattern. The
 747 Atlantic Ocean (within 50°S – 50°N) and the Southern Ocean store more heat than the
 748 other basins, probably associated with the deep convection and subduction processes

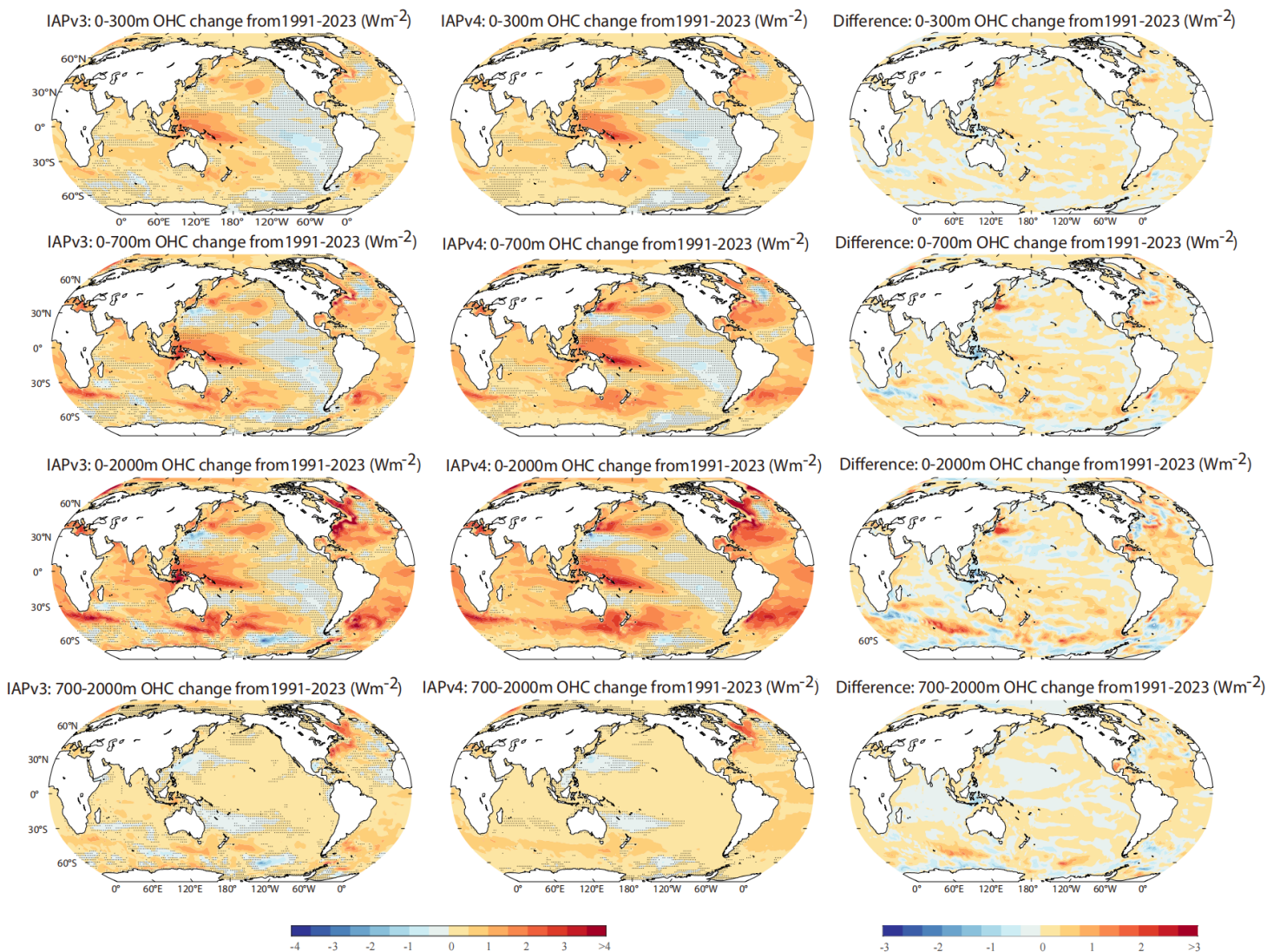
749 effectively transporting heat into the deep layers (Cheng et al., 2022a). The cold spots
 750 mainly include the Northwest Pacific and subpolar North Atlantic Ocean. In particular, the
 751 so-called “warming hole” in the subpolar North Atlantic Ocean can extend to at least 800
 752 m and is responsible for decreased OHC in this region. Some studies have linked this
 753 fingerprint to the slowdown of AMOC (Rahmstorf et al, 2015; Caesar et al., 2018).



755 **Figure 13: Spatial pattern of the OHC trends for 0–300 m, 0–700 m and 0–2000 m,**
 756 **700–2000 m from 1960 to 2023.** The left panels show IAPv3, the middle panels are
 757 IAPv4; the right panels are the difference between IAPv4 and IAPv3.

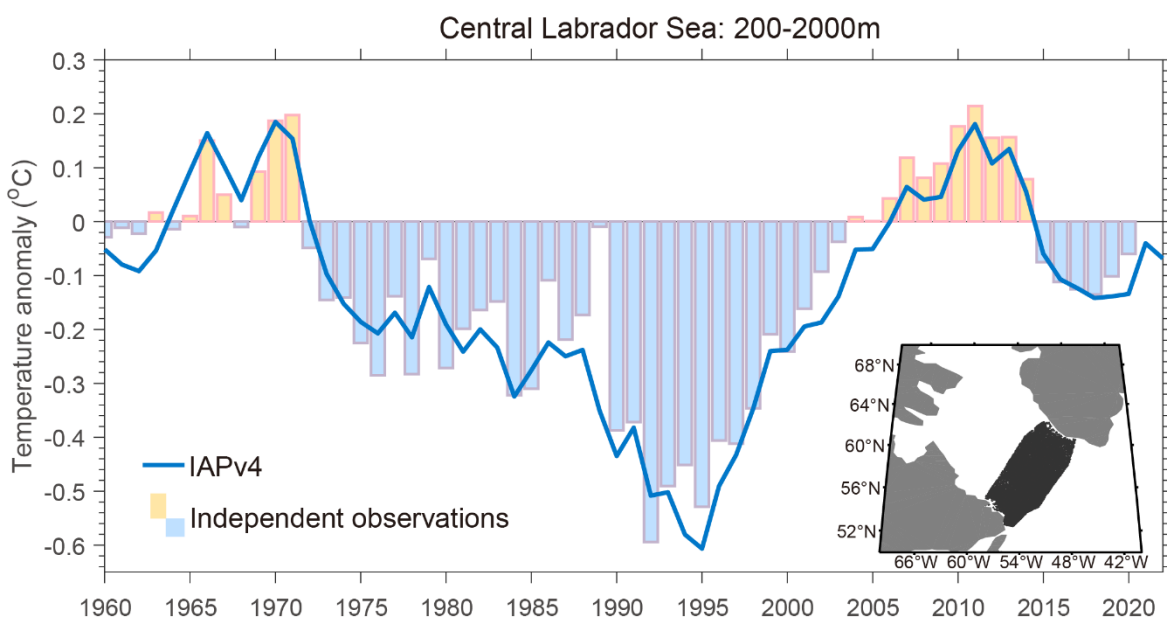
758 For 1991–2023 (Fig. 14), the IAPv4 and IAPv3 pattern is also consistent. A trend
 759 pattern mimicing a negative Pacific Decadal Variability (PDV) phase appears in the Pacific
 760 for the 0–300 m, 0–700 m, and 0–2000 m OHCs. There is a contrast between the warming

761 trend of the tropical western Pacific and the cooling trend of the tropical eastern Pacific.
 762 Some studies have linked this pattern to the natural climate mode (PDV) (England et al.,
 763 2014), but some suggest it is a forced change driven by greenhouse gas increases (Fasullo
 764 and Nerem, 2018; Mann, 2021). Below 700 m, the 1960–2023 and 1991–2023 trend
 765 patterns are similar because deep ocean warming mainly occurs after 1990. Broad warming
 766 in most regions, but subtropical oceans in the West Pacific and South Indian oceans show a
 767 cooling, which is likely related to the subtropical gyre intensification in the North but a
 768 spin-down in the North Pacific Ocean (Zhang et al., 2014).



770 **Figure 14: Spatial pattern of the OHC trends for 0–300 m, 0–700 m, 0–2000 m and**
 771 **700–2000 m from 1991 to 2023.** The left panels show IAPv3, the middle panels are
 772 IAPv4; the right panels are the difference between IAPv4 and IAPv3.

773 Furthermore, the reconstruction of IAPv4 is compared with completely independent
 774 observations in the central Labrador Sea (see Data and Methods section for details;
 775 Yashayaev, 2007; Yashayaev and Loder, 2017) for the 200-2000 m mean temperature time
 776 series (Fig. 15). The direct observations show a substantial decadal variation in the central
 777 Labrador Sea, with negative anomalies 1970-2003 and 2015-2020, and positive anomalies
 778 1963-1972 and 2004-2014. Reconstructed based on data from WOD, IAPv4 can well
 779 represent this decadal variability. The largest difference occurs in 1989, where direct
 780 observations show nearly zero anomaly while IAPv4 shows a big negative anomaly; this
 781 difference is likely caused by using a time window in IAPv4, which has a smoothing effect
 782 on the time series.



783
 784 **Figure 15: Comparison of IAPv4 data with independent observations in the central**
 785 **Labrador Sea (304 -310 °E, 55-61 °N) from 1960 to 2020.** The 200-2000 m averaged
 786 temperature anomaly time series is shown, and the baseline is 1960-2020. The inner box
 787 shows the locations of the independent observations in black dots (showing a total of
 788 49,849 profiles).

789
 790 **3.6 Ocean meridional heat transport**

791 The ocean meridional heat transport (MHT) is fundamental to maintaining the earth's
 792 energy balance. Thus, its change and stability are key to the climate system and its
 793 variability. The direct observations of ocean MHT are only possible in several cross-basin
 794 sections such as RAPID. The ocean MHT can be derived from the OHC and air-sea heat

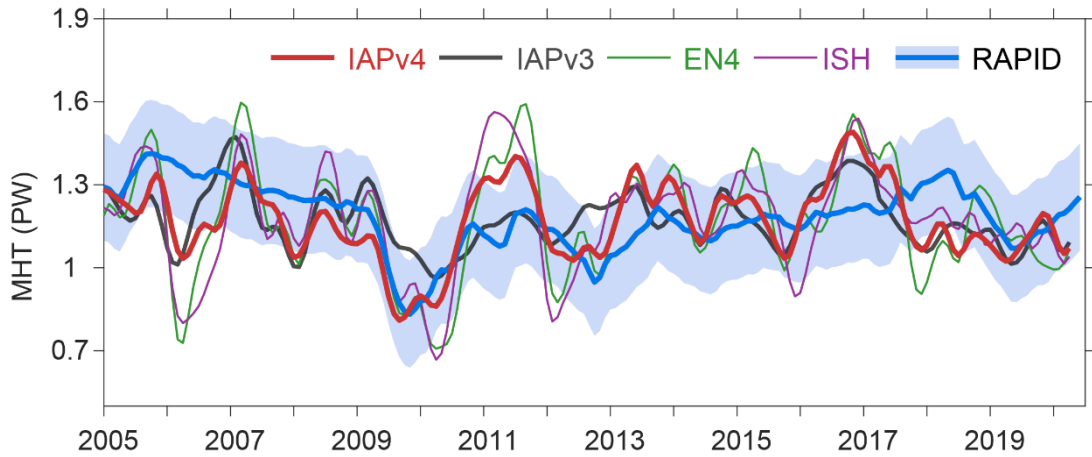
795 flux data (Trenberth and Fasullo, 2017; Trenberth et al., 2019) as follows: we integrate the
 796 OHCT, air-sea heat flux and heat gain/loss by sea ice changes from the North Pole
 797 southward in the Atlantic Ocean, and solve the energy budget equation, the residual at each
 798 latitude is the MHT, i.e.,

$$799 \quad MHT(\varphi) = \int_{\varphi}^{90} \left[F_s + \frac{dOHC}{dt} + Q_{ice} \right] a d\varphi$$

800 Where a is the Earth's radius, φ is latitude, F_s is net surface heat flux, and Q_{ice} is
 801 the heat inferred from the changes of sea ice mass. Consistent with Trenberth et al. (2019),
 802 this study uses the sea ice volume data from the Pan-Arctic Ice Ocean Modeling and
 803 Assimilation System (PIOMAS; Schweiger et al. 2011), and assumes a constant latent heat
 804 of fusion of $3.34 \times 10^5 \text{ J kg}^{-1}$ and a density of ice of 900 kg m^{-3} . Both F_s and OHCT are
 805 important for the MHT derivation: the integrated air-sea heat flux dominates the magnitude
 806 of the MHT, while the OHCT dominates the variability of the MHT (Liu et al., 2020).

807 The comparison between OHC-derived MHT and RAPID data allows one to check
 808 the consistency among various observations. Here, we calculate the Atlantic MHT from
 809 April 2004 to December 2022 using IAPv4 OHC and air-sea net heat flux data (F_s) derived
 810 by TOA net energy flux and atmospheric heat divergence (Fig. 16). F_s is an average of
 811 three available products including MAYER2021 (Mayer et al., 2021) TF2018 (Trenberth et
 812 al., 2019) and the DEEP-C Version 5.0 from Reading University (Liu and Allan, 2022; Liu
 813 et al., 2020). The data are adjusted following Trenberth et al. (2019) approach to ensure
 814 zero MHT on the Antarctica coast. The inferred time series of MHT at 26.5°N from other
 815 OHC data sets (IAPv3, Ishii, and EN4) are also shown in Fig. 16, compared with the
 816 RAPID observations (Johns et al., 2023).

817 The Inferred long-term mean (April 2004–December 2022) MHT from the updated
 818 IAPv4 OHCT (solid red line with the mean transport of 1.18 PW) is identical to the
 819 RAPID observation of $1.18 \pm 0.19 \text{ PW}$. Different OHC datasets cause different inter-
 820 annual variability in the MHT. It is shown that, from 2008 to 2020, the RAPID MHT
 821 agrees best with the IAPv4 estimates with a correlation of 0.52. By comparison, the
 822 correlation coefficients between RAPID and IAPv3, EN4, and Ishii are 0.33, 0.51, and
 823 0.49, respectively. Over the entire period of 2005~2022, the IAPv4 lies mostly within the
 824 RAPID uncertainty envelope.



825

826 **Figure 16: Derived meridional heat transport at 26.5 °N.** The 12-month running mean
 827 northward MHT across 26.5 °N of different data sets compared with results from the
 828 RAPID array in PW. The error bars for RAPID in grey are 1.64 σ .

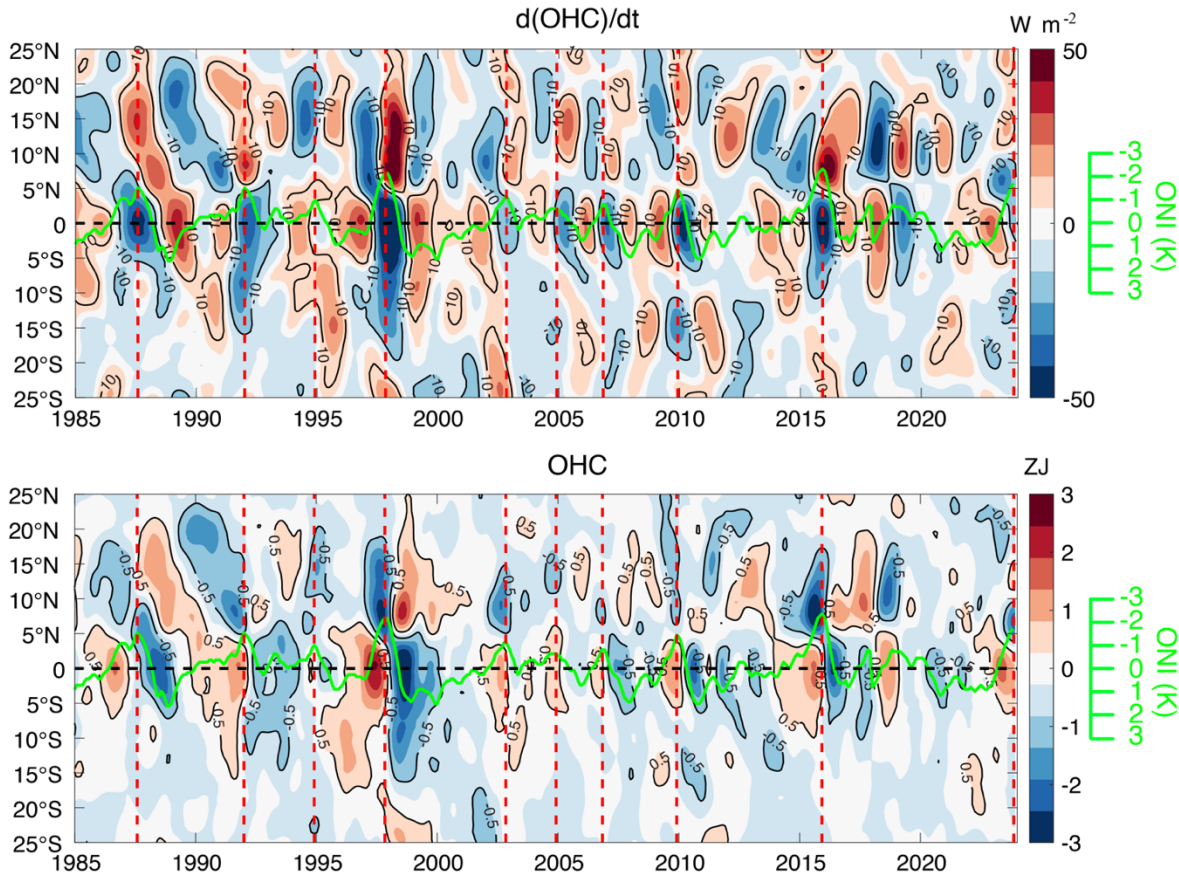
829

830 3.7 Inter-annual variability

831 The year-to-year variation of OHC is strongly influenced by ENSO from global to
 832 regional scales (Cheng et al., 2019; Roemmich and Gilson, 2011). To demonstrate the
 833 change of OHC associated ENSO, Figure 17 shows a Hovmöller diagram of the zonal
 834 upper 2000 m OHC and its change (time derivative of OHC: $d(\text{OHC})/dt$) in the tropical
 835 Pacific Ocean from 1985 to 2023, compared with the Oceanic Niño Index (ONI). It is
 836 evident that both OHC and OHCT are closely correlated with ENSO.

837 Before the onset of El Niño events, there is an accumulation of heat ($d(\text{OHC})/dt > 0$)
 838 in the southern and equatorial tropical Pacific ocean region (20 °S– 5 °N). The positive
 839 tropical Pacific $d\text{OHC}/dt$ leads ONI by ~15 months (with peak correlation >0.5), making it
 840 a precursor of El Niño (Cane and Zebiak 1985; McPhaden, 2012; Lian et al., 2023). In
 841 contrast, heat is redistributed ($d(\text{OHC})/dt < 0$) from the tropical Pacific (20 °S – 5 °N) to
 842 the North Pacific (5 °N – 25 °N) during and after El Niño (Cheng et al., 2019), with a
 843 maximum correlation >0.8 at 5 months after the El Niño peak. The magnitude of the
 844 prominent change can reach up to 50 Wm^{-2} during the 1997–1998 and 2015–2016 extreme
 845 El Niño events. For the other moderate El Niño events, the regional Pacific OHC change
 846 varies around 10–20 Wm^{-2} (Mayer et al., 2018). This typical heat recharge-discharge
 847 paradigm is crucial in ENSO evolution (Jin, 1997). Correspondingly, the zonal OHC
 848 anomalies in the Pacific Ocean show a warming state ($\text{OHC} > 0$) between ~20 °N and
 849 ~5 °S before the peak of El Niño events (with peak correlation >0.7 at 5 months before El

850 Niño peak), followed by a period of cooling (OHC < 0) after the peak of El Niño (with
 851 peak correlation >0.7 at 12 months after El Niño peak). These variations are all physically
 852 meaningful and indicate that IAPv4 represents regional inter-annual variability, especially
 853 associated with ENSO.



854
 855 **Figure 17:** Hovmöller diagrams illustrating the zonal mean (top) upper 2000 m $d(OHC)/dt$
 856 (Wm^{-2}) and (bottom) OHC (ZJ) in each 1° latitude band within $25^\circ S \sim 25^\circ N$ in the
 857 tropical Pacific basin using IAPv4 data. The ONI is shown in green. Vertical dashed lines
 858 denote the peak time of each Niño event.

859

860 3.8 Ocean and Earth Energy Budget

861 The EEI provides a critical quantifier of the Earth's energy flow and climate change.
 862 It is also policy-relevant because it clearly shows the need to stabilize the climate system.
 863 With new T/OHC data, we re-assess the Earth's energy inventory since 1960. The land,
 864 atmosphere, and ice contributions are from the estimates obtained by von Schuckmann et
 865 al. (2023) for 1960-2023 and by Trenberth (2022) for 2015-2019.

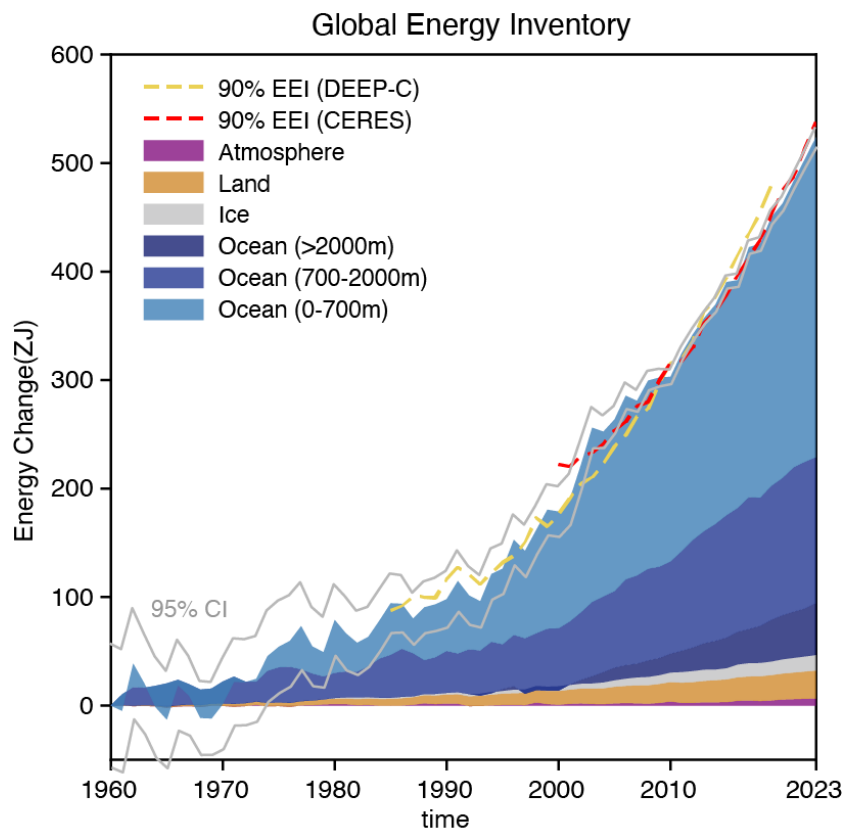
866 It is evident that the earth has been accumulating heat since 1960. The Earth's heat
867 inventory is 524.0 ± 95.6 ZJ from 1960 to 2023 and 260.3 ± 25.3 ZJ from 2005–2023
868 based on our data. The upper 700 m ocean, 700–2000 m, 2000 m-bottom, land, ice, and
869 atmosphere contribute to 59.3%, 24.1%, 7.4%, 5.2%, 2.9%, and 1.1% of the total EEI,
870 respectively, since 1960. The relative contribution has changed with time; for instance,
871 since 1993, the contributions are 53.7% (0–700 m ocean), 24.8% (700–2000 m ocean),
872 12.8% (2000 m–bottom ocean), 4.1% (land), 3.2% (ice), and 1.4% (atmosphere). The land
873 and ice contribution has increased in the recent two decades because of accelerated land
874 and sea ice melting (Comiso et al., 2017; Hugonnet et al., 2021; Minière et al., 2024).
875 From 2005–2019, more reliable land–atmosphere–ice datasets in Trenberth (2022) suggest
876 a non–ocean contribution of 13.4 ZJ. Combined with the results for OHC with IAPv4, the
877 accumulated EEI is 182.5 ZJ with the ocean heat uptake of 169.1 ± 19.7 for 2005–19,
878 consistent with the value of 186.4 ± 23.1 ZJ using the non–ocean contribution data by von
879 Schuckmann et al. (2023).

880 The derived energy inventory has been compared with satellite–based observations at
881 the top of the atmosphere (TOA). Two comparisons are made: (1). integrate the TOA EEI
882 to compare with the energy inventory (Fig. 18); (2) take the time derivative of the annual
883 OHC to compare it with the TOA net radiation flux (Fig. 19). Here we always assume 90%
884 of EEI is stored in the ocean and leads to an increase of OHC (Trenberth et al. 2009;
885 Hansen et al., 2011; von Schuckmann et al., 2020).

886 The first approach avoids calculating the time derivative of OHC, which exacerbates
887 noise in the time series. The net CERES change has been adjusted to 0.71 Wm^{-2} within
888 2005–2015, here we adjust the trend of the integrated CERES data to the IAPv4 OHC
889 trend to make it consistent and then compare the variability difference (Fig. 18). The
890 RMSE between DeepC and IAPv4 is 17.9 ZJ and 15.5 ZJ between CERES and IAPv4. The
891 comparison also indicates that the heat inventory shows a stronger heat increase from 2000
892 to 2005 but too slow heat accumulation during 2005–2010 compared with DeepC and
893 CERES (Fig. 18). This might be due to the data gaps before the Argo network was fully
894 established. DeepC and CERES show stronger heat accumulation since ~2015 than the
895 heat inventory, probably associated with the accelerated abyssal ocean warming found by
896 the Deep-Argo program (Johnson et al., 2019). Furthermore, IAPv4 OHC shows a slightly
897 higher (but consistent within the uncertainty range) Earth's heat uptake compared to von

898 Schuckmann et al. (2023) results by 76.2 ZJ from 1960 to 2020, mainly because the
899 correction of Nansen bottle biases and the updates of XBT and MBT biases in IAPv4 data.

900 The second approach to compare OHC with satellite-based EEI is to calculate the
901 time derivative of OHC. To suppress the month-to-month noises, we estimate annual
902 OHC based on one-year data centered on June (Fig. 19a) and December (Fig. 19b)
903 separately, and then $dOHC/dt$ is calculated with a forward derivative approach based on
904 the annual time series. The annual mean of EEI time series is also used here for
905 comparison (Fig. 19). The IAPv4 and CERES estimates show inter-annual variability with
906 a correlation of 0.44 (the correlation is statistically significant at 90% confidence level,
907 where autocorrelation reduction is taken into account). The higher correlation of IAPv4
908 versus CERES than IAPv3 increases confidence for the new data (correlation of only ~ 0.15
909 for IAPv3). The trend of $dOHC/dt$ is $0.36 \text{ Wm}^{-2} \text{ dec}^{-1}$ from 2005 to 2023, within the
910 uncertainty range of the CERES record ($0.50 \pm 0.47 \text{ Wm}^{-2} \text{ dec}^{-1}$ in Loeb et al., 2021).
911 However, it should be noted that the calculation of $dOHC/dt$ is sensitive to the choices of
912 methods, data products, and time periods because of the noises and variability in the OHC
913 time series. A careful analysis of the trend of $dOHC/dt$ (and EEI) is a research priority.

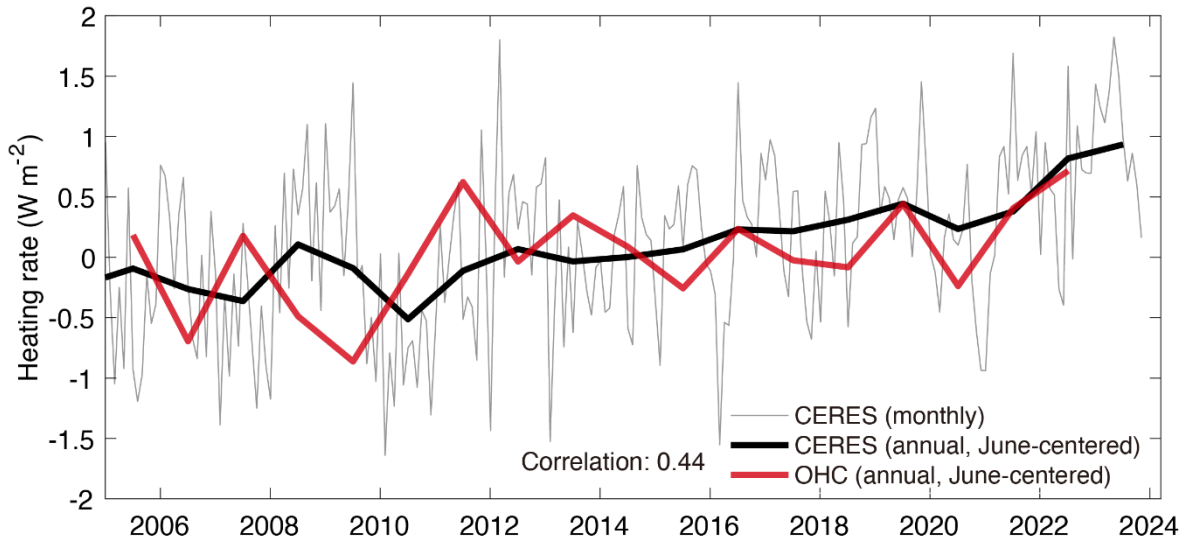


914

915 **Figure 18: The global energy budget from 1960 to 2023.** The atmosphere, land, and ice
916 heat inventory is from von Schuckmann et al., (2023). Integrated EEI from DEEP-C

917 (1985–2018) (Liu and Allan, 2022) and CERES (2001–2023) (Loeb et al., 2021) dataset
 918 are presented by dashed lines for comparison, with the trend adjusted to the IAP estimate
 919 to account for the arbitrary choice of integration constant. 95% Confidence Interval is
 920 presented assuming the independency of different budget components.

921



922

923 **Figure 19: Annual ocean heating rate compared with CERES data.** Both annual OHC
 924 and CERES EEI data are centred in June. The long-term mean is removed for all-time
 925 series.

926

927 3.9 Steric sea level and sea level budget

928 The updated IAPv4 data is used to assess the sea level budget for 1960-2023 in
 929 combination with other data, including IAP salinity data, glaciers, Greenland, Antarctic ice
 930 sheets mass loss from Frederikse et al. (2020) and altimetry sea level record (see Methods
 931 section for details). From 1960 to 2023, the observed GMSL rise is $2.07 \pm 0.55 \text{ mm yr}^{-1}$
 932 (Frederikse et al., 2020), which is derived by combining tide-gauge observations with
 933 estimates of local vertical land motion from permanent Global Positioning System stations
 934 and the difference between tide-gauge and satellite altimetry observations (Frederikse et
 935 al., 2018). During the same period, the sum of contributors (Glaciers, Greenland and
 936 Antarctic ice sheets, land water storage, and steric sea level) yields a mean sea level rise of
 937 $1.87 \pm 0.42 \text{ mm yr}^{-1}$. Thus, the sea level budget can be closed within a 90% confidence
 938 interval. This updated estimate indicates that the steric sea level, Antarctic ice sheet,

939 Greenland ice sheet, glaciers, and land water storage contribute to the total sea level with
940 47.3%, 8.6%, 18.0%, 29.1%, and -3.1%, respectively for 1960-2023.

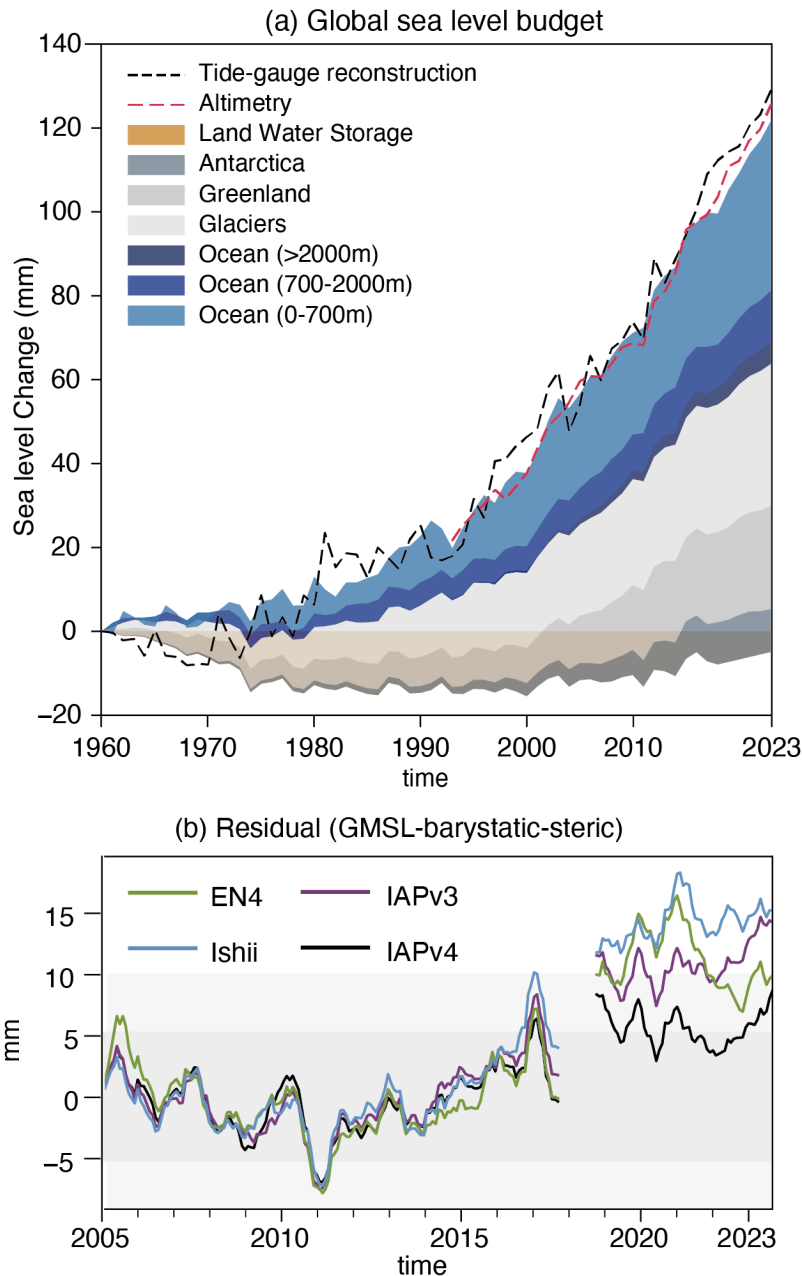
941 To isolate the contribution of the IAPv4 to the sea level budget, we replace the steric
942 sea level estimate in Frederikse et al., (2020) with IAPv4 and re-assess the sea level budget
943 for 1960-2018, 1993-2018 and 2005-2018, and the other components are identical to
944 Frederikse et al. (2020). Two metrics are used to quantify the performance of sea level
945 budget closure: the mean residual error and the temporal root mean square error (RMSD)
946 between the observed GMSL and the sum of contributions. We find that the residual sea
947 level budget based on IAPv4 is 0.20 ± 0.53 , 0.11 ± 0.34 , 0.47 ± 0.56 mm yr⁻¹ for 1960-
948 2018, 1993-2018 and 2005-2018, respectively. These mean residual errors are all smaller
949 than presented in Frederikse et al., (2020), which showed a residual error of 0.29 ± 0.57 ,
950 0.20 ± 0.34 and 0.54 ± 0.58 mm yr⁻¹ for 1960-2018, 1993-2018 and 2005-2018,
951 respectively. The RMSD using IAPv4 (or using steric sea level in Frederikse et al., 2020)
952 is 5.59 (5.35), 4.89 (5.33) and 4.21 (4.51) mm for the above-mentioned three periods,
953 respectively. Therefore, both metrics show that IAPv4 data improves the sea level budget
954 in three typical periods.

955 A similar test is done with the IPCC-AR6 sea level budget estimate (Gulev et al.,
956 2021): the thermosteric sea level estimate in IPCC-AR6 is replaced by IAPv4, and the sea
957 level budget is re-assessed for 1993-2018. IAPv4 suggests a larger thermosteric sea level
958 rise of 1.43 ± 0.16 for 1993-2018 than IPCC (1.31 ± 0.36 mm yr⁻¹) from 1993-2018.
959 Replacing the thermosteric sea level estimate by IAPv4 reduces the mean residual error
960 from 0.40 ± 0.57 to 0.28 ± 0.48 mm yr⁻¹. This suggests that the stronger warming since the
961 1993 revealed by IAPv4 than assessed in IPCC-AR6 (Gulve et al., 2021), seems more
962 realistic.

963 After 2002, the GRACE satellite supported the direct observation of barystatic sea
964 level, which is the sum of the sea level change due to the land water storage, Antarctica ice
965 sheet, Greenland ice sheet, and glaciers. The sea level budget can be obtained by
966 comparing altimetry-based GMSL with the barystatic sea level observed by GRACE and
967 the steric sea level. It is evident that the sea level budget can be closed between 2002 and
968 2015 with ± 5 mm residual errors (Fig. 20b). However, after ~ 2015 , the sum of steric and
969 barystatic sea level is smaller than the total sea level rise for all ocean temperature
970 products. Previous studies have attributed this misclosure to salinity data biases (Barnoud
971 et al., 2021), altimetry data errors (Barnoud et al., 2023), and GRACE data errors (Wang et

972 al., 2021). The steric sea level inferred from IAPv4 showed a lower residual (~5 mm)
973 between 2005–2023 than ISH and EN4 data (10~20 mm), indicating that the temperature
974 data might be partly responsible for lack of closure of sea level budget since ~2015. This
975 suggests again that the stronger warming in recent years, as indicated by IAPv4, is more
976 realistic. As discussed in Section 3.4, the QC is mainly responsible for the increased
977 warming of IAPv4 compared with IAPv3 since ~2015 (Fig. 11).

978 Many traditional QC procedures use a static climatological range check to filter out
979 outliers, which does not account for the increase of extreme events with climate change
980 and removes too many extreme (positive) values during the recent period. Thus, we
981 strongly recommend that data product generation groups revisit the QC procedure.
982 Furthermore, as the stronger long-term OHC trends since ~1960 in IAPv4 than in IAPv3
983 are mainly attributed to the bias corrections for Nansen Bottle, MBT, and XBT data, it is
984 also recommended that international groups to revisit the biases in ocean observations.
985



986

987 **Figure 20: (a) The sea level budget from 1960 to 2023.** Observed global mean sea level
 988 for 1960–2023 and the individual contributions from land water storage, Antarctica,
 989 Greenland and Glaciers (Frederikse et al., 2020). The budget is relative to a 1960 baseline.
 990 Here, the land water storage and Glaciers data are through 2018, and a linear extrapolation
 991 is made for 2019–2023. Antarctica ice sheet and Greenland ice sheet changes are estimated
 992 by GRACE after 2018. Tide gauge after 2018 are updated by altimetry. Altimetry sea level
 993 is shown in red dashed line for comparison. (b) Sea level budget residual time series since
 994 2005. The residual of GMSL minus barystatic and steric sea level. The seasonal cycle is
 995 reduced based on 2005–2015 climatology. 6–month running means are shown here to
 996 reduce the noise.

997

998 **4. Data availability**

999 IAPv4 global ocean temperature product is available at

1000 <http://dx.doi.org/10.12157/IOCAS.20240117.002> (Cheng et al., 2024a) and

1001 <http://www.ocean.iap.ac.cn/>.

1002 IAPv4 global ocean heat content product is available at

1003 <http://dx.doi.org/10.12157/IOCAS.20240117.001> (Cheng et al., 2024b) and

1004 <http://www.ocean.iap.ac.cn/>.

1005 The code used in this paper includes data quality control, and the resultant dataset is

1006 available at <http://www.ocean.iap.ac.cn/>.

1007

1008 The data used in this study (but not generated by this work) are listed below. IAP data are

1009 available at <http://www.ocean.iap.ac.cn/>. The NCEI/NOAA data are available at

1010 (<https://www.ncei.noaa.gov/products/climate-data-records/global-ocean-heat-content>). ISH

1011 data from (<https://climate.mri-jma.go.jp/pub/ocean/ts/v7.2/>). The EN4 data

1012 (<https://www.metoffice.gov.uk/hadobs/en4/index.html>) For SST: ERSSTv5

1013 (<https://www1.ncdc.noaa.gov/pub/data/cmb/ersst/v5/netcdf/>); COBE2

1014 (<https://psl.noaa.gov/data/gridded/data.cobe2.html>); and HadSST3

1015 (<https://www.metoffice.gov.uk/hadobs/hadsst3/data/download.html>). For sea level data:

1016 AVISO+ GMSL ([https://www.aviso.altimetry.fr/en/data/products/ocean-indicators-](https://www.aviso.altimetry.fr/en/data/products/ocean-indicators-products/mean-sea-level.html#c15723)

1017 [products/mean-sea-level.html#c15723](https://www.aviso.altimetry.fr/en/data/products/ocean-indicators-products/mean-sea-level.html#c15723)), JPL GRACE ([https://grace.jpl.nasa.gov/data/get-](https://grace.jpl.nasa.gov/data/get-data/jpl_global_mascons/)

1018 [data/jpl_global_mascons/](https://grace.jpl.nasa.gov/data/get-data/jpl_global_mascons/)), the data in Frederikse et al., (2020) from

1019 (<https://zenodo.org/records/3862995>). The data in von Schuckmann et al., (2023)

1020 (https://www.wdc-climate.de/ui/entry?acronym=GCOS_EHI_1960-2020). Argo data were

1021 collected and made freely available by the International Argo Program and the national

1022 programs that contribute to it (<https://argo.ucsd.edu>, <https://www.ocean-ops.org>). DEEP-C

1023 data from <https://doi.org/10.17864/1947.000347>; CERES data ([1024 \[tool.larc.nasa.gov/ord-tool/jsp/EBAFTOA41Selection.jsp\]\(https://ceres-tool.larc.nasa.gov/ord-tool/jsp/EBAFTOA41Selection.jsp\)\); GIOMAS ice volume data](https://ceres-</p></div><div data-bbox=)

1025 from (https://psc.apl.washington.edu/zhang/Global_seaice/data.html). SCRIPPS data from

1026 (http://sio-argo.ucsd.edu/RG_Climatology.html); BOA data from

1027 (<https://argo.ucsd.edu/data/argo-data-products/>).

1028

1029 **5. Summary and Discussion**

1030 This paper introduces a new version of the ocean temperature and heat content
1031 gridded products and describes the data source and data processing techniques in detail.
1032 The key technical advances include the new QC, new or updated XBT/MBT/Bottle/APB
1033 bias corrections, new ocean temperature climatology, improved mapping approach, and
1034 grid-cell ocean volume corrections. These data and technical advances allow a better
1035 estimate of long-term ocean temperature and heat content changes since the mid-1950s
1036 from the sea surface down to 2000 m. We show that the new data product could better
1037 close the sea level and energy budgets than IAPv3. For rates of change, compared with
1038 CERES, the IAPv4 also shows a better correlation from 2005 to 2023 than IAPv3.

1039 Despite several marked improvements, issues needing further investigation remain.
1040 Although inter-annual and decadal-scale changes of satellite-based EEI and observational
1041 OHC are generally consistent, a mismatch remains between EEI and OHC for their month-
1042 to-month variation, as the monthly variation of OHC is still much larger than implied by
1043 EEI. There are several possibilities, in our opinion: first, there is substantial heat storage
1044 and release for land and ice monthly, which needs to be accurately quantified; second, the
1045 accuracy of OHC estimate on a monthly basis still needs to be improved for month-to-
1046 month variation because of the limited data coverage; third, the EEI observed by CERES
1047 also suffers from sampling biases on a monthly basis (Loeb et al., 2009). Thus, a better
1048 understanding of the monthly variation of OHC and EEI is still a research priority. Besides,
1049 the failure to close the 2015-2023 sea level budget indicates that the underlying data still
1050 has bias problems, which need to be explored and resolved.

1051 Second, the application of CODC-QC in IAPv4 leads to a stronger ocean warming
1052 rate in the past decade than WOD-QC used in IAPv3 because WOD-QC removes more
1053 positive temperature anomalies than CODC-QC. This could imply that the rate of increase
1054 in OHC is still slightly underestimated and deserves an in-depth investigation. Several
1055 fundamental questions must be answered: first, are there still real temperature extremes
1056 being removed by CODC-QC, such as in small warm/cold eddies? Are the extremes well
1057 sampled by the current observation system? If not, what is the impact? Moreover, it is clear
1058 that the high latitudes where sea ice occurs are not well sampled and need more attention.

1059 Third, during the development of the data product, we discovered that much metadata
1060 relating to the profiles in the World Ocean Database is missing and that much existing
1061 metadata is incorrect, also giving rise to duplicate profiles, putting a strain on the overall

1062 quality of a database of oceanic observations. More than ever, long-term concerted efforts
1063 are needed to eliminate duplicate profiles and identify and correct missing metadata using
1064 statistical methods, expert control, or machine learning techniques. For example, the
1065 International Quality-Controlled Database (IQuOD) group is coordinating some activities
1066 related to data processing techniques, uncertainty quantification, and improving the overall
1067 quality of ocean data (Cowley et al., 2021).

1068 Fourth, the deep ocean changes below 2000 m are estimated based on the currently
1069 available data, including data from hydrological sections and Deep-Argo. IAP mapping
1070 technique is applied. Because of the lack of independent observations with global ocean
1071 coverage, evaluating the deep ocean change estimate is still dicey. Thus, the below-2000 m
1072 estimate should be used with caution, as also indicated in previous estimates (Purkey and
1073 Johnson, 2010; Desbruyères et al., 2017; Good et al., 2013). A community-agreed
1074 evaluation approach for the deep ocean changes is critically needed. Besides, other
1075 mapping techniques deserving further investigation include interpolation on isopycnal
1076 surfaces (Palmer and Haines, 2009).

1077 Furthermore, the quantification of uncertainty for *in situ* measurements, gridded
1078 T/OHC values, and the global OHC estimates need to be improved. IAPv4 only accounts
1079 for the instrumental error and sampling/mapping error. In the future, comprehensive
1080 quantification of other uncertainty sources will be made, including the choice of
1081 climatology, vertical interpolation, XBT/MBT/APB/Bottle corrections, etc. It is also
1082 necessary to analyze the correlation between these error sources. This also helps to
1083 understand regions with larger uncertainty for OHC estimates, which supports the design
1084 of the global ocean observing system.

1085

1086 **Author contributions.** L.C. has worked on this study's conceptualization, coordination,
1087 methodologies, and writing the manuscript. Z.T. worked on *in situ* observation collections,
1088 metadata format, and the automated quality control procedure (CODC-QC) development.
1089 Y.P. has worked on calculating and comparing the OHC annual cycle, the mixed layer
1090 depth, and the MHT among different data sets. V.G. worked on bias correction schemes for
1091 MBT, APB, and bottle data and on developing the automated quality control procedure.
1092 H.Y. worked on the analysis of inter-annual variability. J.D. has worked on OHC trend
1093 calculation and analysis. G.L. worked on SST calculation and its analysis. H. Z. worked on
1094 global energy and sea level budget calculations and analyses. Y.L. and Y.J. worked on the

1095 volume correction. All authors have contributed to formal analysis, data validation, and
1096 editing of the original draft.

1097

1098 **Acknowledgement and Funding.** The IAP/CAS analysis is supported by the National
1099 Natural Science Foundation of China (Grant no. 42122046, 42076202, 42206208,
1100 42261134536), Strategic Priority Research Program of the Chinese Academy of Sciences
1101 (Grant no. XDB42040402), the new Cornerstone Science Foundation through the
1102 XPLOER PRIZE, DAMO Academy Young Fellow, Youth Innovation Promotion
1103 Association, Chinese Academy of Sciences, National Key Scientific and Technological
1104 Infrastructure project “Earth System Science Numerical Simulator Facility” (EarthLab),
1105 the Young Talent Support Project of Guangzhou Association for Science and Technology.
1106 The calculations in this study were carried out on the ORISE Supercomputer. Some data
1107 were collected onboard of R/V Shiyan 6 implementing the Open Research Cruise
1108 NORC2022-10+NORC2022-303 supported by NSFC Shiptime Sharing Projects
1109 42149910. NCAR is sponsored by the US National Science Foundation. We acknowledge
1110 the World Climate Research Programme’s Working Group on Coupled Modelling, which
1111 is responsible for CMIP, and we thank the climate modeling groups for producing and
1112 making their model output available through the Earth System Grid Federation. The Argo
1113 Program is part of the Global Ocean Observing System.

1114

1115 **Competing interests.** The contact author has declared that none of the authors has any
1116 competing interests.

1117

1118 **References**

- 1119 Abraham, J. P., Cheng, L., Mann, M. E., Trenberth, K., and von Schuckmann, K.: The
1120 ocean response to climate change guides both adaptation and mitigation efforts.
1121 Atmospheric and Oceanic Science Letters, 15, 100221,
1122 <https://doi.org/10.1016/j.aosl.2022.100221>, 2022.
- 1123 Abraham, J. P., and Cheng, L.: Intersection of Climate Change, Energy, and Adaptation.
1124 Energies. 15(16), 5886; <https://doi.org/10.3390/en15165886>, 2022.
- 1125 Abraham, J. P., Baringer, M., Bindoff, N. L., Boyer, T., Cheng, L. J., Church, J. A.,
1126 Conroy, J. L., Domingues, C. M., Fasullo, J. T., Gilson, J., Goni, G., Good, S. A.,

1127 Gorman, J. M., Gouretski, V., Ishii, M., Johnson, G. C., Kizu, S., Lyman, J. M.,
1128 Macdonald, A. M., Minkowycz, W. J., Moffitt, S. E., Palmer, M. D., Piola, A. R.,
1129 Reseghetti, F., Schuckmann, K., Trenberth, K. E., Velicogna, I., and Willis, J. K.: A
1130 review of global ocean temperature observations: Implications for ocean heat content
1131 estimates and climate change, *Rev. Geophys.*, 51, 450–483,
1132 <https://doi.org/10.1002/rog.20022>, 2013.

1133 Argo: Argo float data and metadata from Global Data Assembly Centre (Argo GDAC).
1134 SEANO, 2000.

1135 Bagnell, A., and DeVries, T.: 20(th) century cooling of the deep ocean contributed to
1136 delayed acceleration of Earth's energy imbalance. *Nat. Comm.*, 12, 4604,
1137 <https://doi.org/10.1038/s41467-021-24472-3>, 2021.

1138 Barker, P. M., and McDougall, T. J.: Two Interpolation Methods Using Multiply-Rotated
1139 Piecewise Cubic Hermite Interpolating Polynomials. *J. Atmos. Ocean Technol.*, 37,
1140 605-619, <https://doi.org/10.1175/JTECH-D-19-0211.1>, 2020.

1141 Barnoud, A., Pfeffer, J., Cazenave, A., Fraudeau, R., Rousseau, V., and Ablain, M.:
1142 Revisiting the global mean ocean mass budget over 2005–2020. *Ocean Science*, 19,
1143 321-334, <https://doi.org/10.5194/os-19-321-2023>, 2023.

1144 Barnoud, A., Pfeffer, J., Guérou, A., Frery, M.-L., Siméon, M., Cazenave, A., Chen, J.,
1145 Llovel, W., Thierry, V., Legeais, J.-F., and Ablain, M.: Contributions of Altimetry
1146 and Argo to Non-Closure of the Global Mean Sea Level Budget Since 2016.
1147 *Geophys Res Lett*, 48, e2021GL092824, <https://doi.org/10.1029/2021GL092824>,
1148 2021.

1149 Bindoff, N. L., Cheung, W. W. L., Kairo, J. G., Arístegui, J., Guinder, V. A., Hallberg, R.,
1150 Hilmi, N., Jiao, N., and Karim, M. S.: Changing Ocean, Marine Ecosystems, and
1151 Dependent Communities. In *IPCC Special Report on the Ocean and Cryosphere in a
1152 Changing Climate* [H.-O. Pörtner, D.C. Roberts, V. Masson-Delmotte, P. Zhai, M.
1153 Tignor, E. Poloczanska, K. Mintenbeck, A. Alegría, M. Nicolai, A. Okem, J. Petzold,
1154 B. Rama, N.M. Weyer (eds.)], Cambridge University Press, Cambridge, UK and
1155 New York, NY, USA, pp. 447–587. <https://doi.org/10.1017/9781009157964.007>,
1156 2019.

1157 Boyer, T., Domingues, C. M., Good, S. A., Johnson, G. C., Lyman, J. M., Ishii, M.,
1158 Gouretski, V., Willis, J. K., Antonov, J., Wijffels, S., Church, J. A., Cowley, R., and
1159 Bindoff, N. L.: Sensitivity of Global Upper Ocean Heat Content Estimates to

1160 Mapping Methods, XBT Bias Corrections, and Baseline Climatologies, *J. Climate*,
1161 29, 4817–4842, <https://doi.org/10.1175/JCLI-D-15-0801.1>, 2016.

1162 Caesar, L., Rahmstorf, S., Robinson, A., Feulner, G., and Saba, V.: Observed fingerprint of
1163 a weakening Atlantic Ocean overturning circulation. *Nature*, 556, 191-196,
1164 <https://doi.org/10.1038/s41586-018-0006-5>, 2018.

1165 Cane, M. A., and Zebiak, S. E.: A theory for El Niño and the southern oscillation. *Science*,
1166 228, 1085-1087, <https://doi.org/10.1126/science.228.4703.1085>, 1985.

1167 Cheng, L.: Sensitivity of Ocean Heat Content to Various Instrumental Platforms in Global
1168 Ocean Observing System. *Ocean-Land-Atmosphere Research*, 0,
1169 <https://doi.org/10.34133/olar.0037>, 2024a.

1170 Cheng, L., and Zhu, J.: Uncertainties of the Ocean Heat Content Estimation Induced by
1171 Insufficient Vertical Resolution of Historical Ocean Subsurface Observations. *J.*
1172 *Atmos. Ocean Technol.*, 31, 1383-1396, [https://doi.org/10.1175/JTECH-D-13-](https://doi.org/10.1175/JTECH-D-13-00220.1)
1173 [00220.1](https://doi.org/10.1175/JTECH-D-13-00220.1), 2014.

1174 Cheng, L., and Zhu, J.: Influences of the Choice of Climatology on Ocean Heat Content
1175 Estimation. *J. Atmos. Ocean Technol.*, 32, 388-394, [https://doi.org/10.1175/JTECH-](https://doi.org/10.1175/JTECH-D-14-00169.1)
1176 [D-14-00169.1](https://doi.org/10.1175/JTECH-D-14-00169.1), 2015.

1177 Cheng, L., and Zhu, J.: Benefits of CMIP5 Multimodel Ensemble in Reconstructing
1178 Historical Ocean Subsurface Temperature Variations. *J. Climate*, 29, 5393-5416,
1179 <https://doi.org/10.1175/JCLI-D-15-0730.1>, 2016.

1180 Cheng, L., Zhu, J., Cowley, R., Boyer, T., and Wijffels, S.: Time, Probe Type, and
1181 Temperature Variable Bias Corrections to Historical Expendable Bathythermograph
1182 Observations. *J. Atmos. Ocean. Technol.*, 31, 1793-1825,
1183 <https://doi.org/10.1175/jtech-d-13-00197.1>, 2014.

1184 Cheng, L., Abraham, J., Goni, G., Boyer, T., Wijffels, S., Cowley, R., Gouretski, V.,
1185 Reseghetti, F., Kizu, S., Dong, S., Bringas, F., Goes, M., Houpert, L., Sprintall, J.,
1186 and Zhu, J.: XBT Science: Assessment of Instrumental Biases and Errors, *B. Am.*
1187 *Meteorol. Soc.*, 97, 924–933, <https://doi.org/10.1175/BAMS-D-15-00031.1>, 2016.

1188 Cheng, L., Trenberth, K. E., Fasullo, J., Boyer, T., Abraham, J., and Zhu, J.: Improved
1189 estimates of ocean heat content from 1960 to 2015. *Sci. Adv.*, 3, e1601545,
1190 <https://doi.org/10.1126/sciadv.1601545>, 2017.

1191 Cheng, L., Trenberth, K. E., Fasullo, J. T., Mayer, M., Balmaseda, M., and Zhu, J.:
1192 Evolution of Ocean Heat Content Related to ENSO. *J. Climate*, 32, 3529-3556,
1193 <https://doi.org/10.1175/jcli-d-18-0607.1>, 2019.

1194 Cheng, L., Trenberth, K. E., Gruber, N., Abraham, J. P., Fasullo, J. T., Li, G., Mann, M. E.,
1195 Zhao, X., and Zhu, J.: Improved Estimates of Changes in Upper Ocean Salinity and
1196 the Hydrological Cycle. *J. Climate*, 33, 10357-10381, [https://doi.org/10.1175/JCLI-](https://doi.org/10.1175/JCLI-D-20-0366.1)
1197 [D-20-0366.1](https://doi.org/10.1175/JCLI-D-20-0366.1), 2020.

1198 Cheng, L., von Schuckmann, K., Abraham, J. P., Trenberth, K. E., Mann, M. E., Zanna, L.,
1199 England, M. H., Zika, J. D., Fasullo, J. T., Yu, Y., Pan, Y., Zhu, J., Newsom, E. R.,
1200 Bronselaer, B., and Lin, X.: Past and future ocean warming. *Nat. Rev. Earth Env.*, 3,
1201 776-794, <https://doi.org/10.1038/s43017-022-00345-1>, 2022a.

1202 Cheng, L., Foster, G., Hausfather, Z., Trenberth, K. E., and Abraham, J.: Improved
1203 quantification of the rate of ocean warming. *J. Climate*, 35, 4827–4840,
1204 <https://doi.org/10.1175/jcli-d-20-0366.1>, 2022b.

1205 Cheng, L., Tan, Z., Pan, Y., Zheng, H., Zhu, Y., Wei, W., Du, J., Li, G., Ye, H., Gourteski,
1206 V.: IAP temperature 1° gridded analysis product (IAPv4),
1207 <http://dx.doi.org/10.12157/IOCAS.20240117.002>, 2024a.

1208 Cheng, L., Tan, Z., Pan, Y., Zheng, H., Zhu, Y., Wei, W., Du, J., Li, G., Ye, H., Gourteski,
1209 V.: IAP global ocean heat content 1° gridded analysis product (IAPv4),
1210 <http://dx.doi.org/10.12157/IOCAS.20240117.001>, 2024b.

1211 Chu, P. C., and Fan, C.: Global climatological data of ocean thermohaline parameters
1212 derived from WOA18. *Scientific Data*, 10, 408, [https://doi.org/10.1038/s41597-023-](https://doi.org/10.1038/s41597-023-02308-7)
1213 [02308-7](https://doi.org/10.1038/s41597-023-02308-7), 2023.

1214 Comiso, J. C., Meier, W. N., and Gersten, R.: Variability and trends in the Arctic Sea ice
1215 cover: Results from different techniques. *J. Geophys. Res.- Oceans*, 122, 6883-6900,
1216 <https://doi.org/10.1002/2017JC012768>, 2017.

1217 Cowley, R., Killick, R. E., Boyer, T., Gouretski, V., Reseghetti, F., Kizu, S., Palmer, M.
1218 D., Cheng, L., Storto, A., Le Menn, M., Simoncelli, S., Macdonald, A. M., &
1219 Domingues, C. M.: International Quality-Controlled Ocean Database (iQuOD) v0.1:
1220 The Temperature Uncertainty Specification. *Front. Mar. Sci.*, 8,
1221 <https://doi.org/10.3389/fmars.2021.689695>, 2021.

1222 Dangendorf, S., Frederikse, T., Chafik, L., Klinck, J. M., Ezer, T., and Hamlington, B. D.:
1223 Data-driven reconstruction reveals large-scale ocean circulation control on coastal
1224 sea level. *Nat. Clim. Change*, 11, 514-520, [https://doi.org/10.1038/s41558-021-](https://doi.org/10.1038/s41558-021-01046-1)
1225 [01046-1](https://doi.org/10.1038/s41558-021-01046-1), 2021.

1226 de Boyer Montégut, C., Madec, G., Fischer, A. S., Lazar, A., and Iudicone, D.: Mixed
1227 layer depth over the global ocean: An examination of profile data and a profile-based

1228 climatology. *J. Geophys. Res.- Oceans*, 109, <https://doi.org/10.1029/2004JC002378>,
1229 2004.

1230 Desbruyères, D., McDonagh, E. L., King, B. A. & Thierry, V. Global and full-depth ocean
1231 temperature trends during the early twenty-first century from Argo and repeat
1232 hydrography. *J. Clim.* 30, 1985–1997, 2017.

1233 England, M. H., McGregor, S., Spence, P., Meehl, G. A., Timmermann, A., Cai, W.,
1234 Gupta, A. S., McPhaden, M. J., Purich, A., & Santoso, A.: Recent intensification of
1235 wind-driven circulation in the Pacific and the ongoing warming hiatus. *Nat. Clim.*
1236 *Change*, 4, 222-227, <https://doi.org/10.1038/nclimate2106>, 2014.

1237 Fasullo, J. T., and Nerem, R. S.: Altimeter-era emergence of the patterns of forced sea-
1238 level rise in climate models and implications for the future. *P. Natl. Acad. Sci.*, 115,
1239 12944-12949, <https://doi.org/10.1073/pnas.1813233115>, 2018.

1240 Frederikse, T., Jevrejeva, S., Riva, R. E. M. and Dangendorf, S.: A Consistent Sea-Level
1241 Reconstruction and Its Budget on Basin and Global Scales over 1958–2014. *J.*
1242 *Climate*, 31, 1267–1280, <https://doi.org/10.1175/JCLI-D-17-0502.1>, 2018.

1243 Frederikse, T., Landerer, F., Caron, L., Adhikari, S., Parkes, D., Humphrey, V. W.,
1244 Dangendorf, S., Hogarth, P., Zanna, L., Cheng, L., and Wu, Y.-H.: The causes of sea
1245 level rise since 1900. *Nature*, 584, 393-397, <https://doi.org/10.1038/s41586-020->
1246 2591-3, 2020.

1247 Garcia, H. E., Boyer, T. P., Locarnini, R. A., Baranova, O. K., and Zweng, M. M.: World
1248 Ocean Database 2018: User’s Manual., T. E. A.V. Mishonov, NOAA, Silver Spring,
1249 MD., Ed. , 2018

1250 Goni, G. J., Sprintall, J., Bringas, F., Cheng, L., Cirano, M., Dong, S., Domingues, R.,
1251 Goes, M., Lopez, H., Morrow, R., Rivero, U., Rossby, T., Todd, R. E., Trinanés, J.,
1252 Zilberman, N., Baringer, M., Boyer, T., Cowley, R., Domingues, Hutchinson, K.,
1253 Kramp, M., Mata, M. M., Reseghetti, F., Sun, C., Bhaskar Tvs U., Volkov, D.: More
1254 Than 50 Years of Successful Continuous Temperature Section Measurements by the
1255 Global Expendable Bathythermograph Network, Its Integrability, Societal Benefits,
1256 and Future. *Fron. Mar. Sci.*, 6, <http://dx.doi.org/10.3389/fmars.2019.00452>, 2019.

1257 Good, S. A., Martin, M. J., and Rayner, N. A.: EN4: Quality controlled ocean temperature
1258 and salinity profiles and monthly objective analyses with uncertainty estimates. *J.*
1259 *Geophys. Res. Oceans*, 118, 6704-6716, <https://doi.org/10.1002/2013jc009067>, 2013.

1260 Gouretski, V., and Koltermann, K. P.: How much is the ocean really warming? *Geophys.*
1261 *Res. Lett.*, 34, L01610, <https://doi.org/10.1029/2006GL027834>, 2007.

1262 Gouretski, V. and Reseghetti, F.: On depth and temperature biases in bathythermograph
1263 data: Development of a new correction scheme based on analysis of a global ocean
1264 database, *Deep Sea Res.*, 57, 6, 812-833, <https://doi.org/10.1016/j.dsr.2010.03.011>,
1265 2010.

1266 Gouretski, V., and Cheng, L.: Correction for Systematic Errors in the Global Dataset of
1267 Temperature Profiles from Mechanical Bathythermographs. *J. Atmos. Ocean.
1268 Technol.*, 37, 841-855, <https://doi.org/10.1175/jtech-d-19-0205.1>, 2020.

1269 Gouretski, V., Cheng, L., and Boyer, T.: On the Consistency of the Bottle and CTD Profile
1270 Data. *J. Atmos. Ocean Technol.*, 39, 1869-1887, [https://doi.org/10.1175/JTECH-D-
1271 22-0004.1](https://doi.org/10.1175/JTECH-D-22-0004.1), 2022.

1272 Gouretski, V., Roquet, F., and Cheng, L.: Measurement biases in ocean temperature
1273 profiles from marine mammal data loggers. *J. Atmos. Ocean Technol.*, submitted,
1274 2024.

1275 Gouretski, V., Kennedy, J., Boyer, T., and Köhl, A.: Consistent near-surface ocean
1276 warming since 1900 in two largely independent observing networks. *Geophys. Res.
1277 Lett.*, 39, <https://doi.org/10.1029/2012GL052975>, 2012.

1278 Gouretski V, Koltermann K P. 2004. WOCE global hydrographic clima- tology. *Berichte
1279 des BSH*, 35: 1–52.

1280 Gulev, S. K., Thorne, P. W., Ahn, J., Dentener, F. J., Domingues, C. M., Gerland, S.,
1281 Gong, D., Kaufman, D. S., Nnamchi, H. C., Quaas, J., Rivera, J. A., Sathyendranath,
1282 S., Smith, S. L., Trewin, B., Schuckmann, K. von, and Vose, R. S.: Changing State
1283 of the Climate System Supplementary Material, in: *Climate Change 2021: The
1284 Physical Science Basis. Contribution of Working Group I to the Sixth Assessment
1285 Report of the Intergovernmental Panel on Climate Change*, edited by: Masson-
1286 Delmotte, V., Zhai, P., Pirani, A., Connors, S. L., Péan, C., Berger, S., Caud, N.,
1287 Chen, Y., Goldfarb, L., Gomis, M. I., Huang, M., Leitzell, K., Lonnoy, E., Matthews,
1288 J. B. R., Maycock, T. K., Waterfield, T., Yelekçi, O., Yu, R., and Zhou, B.,
1289 Cambridge University Press, Cambridge, United Kingdom and New York, NY,
1290 USA, 287– 422, <https://doi.org/10.1017/9781009157896.004>, 2021.

1291 Hakuba, M. Z., Frederikse, T., and Landerer, F. W.: Earth’s Energy Imbalance From the
1292 Ocean Perspective (2005–2019), *Geophys. Res. Lett.*, 48, e2021GL093624,
1293 <https://doi.org/10.1029/2021GL093624>, 2021.

1294 Hansen, J., Sato, M., Kharecha, P., and von Schuckmann, K.: Earth's energy imbalance and
1295 implications. *Atmos. Chem. Phys.*, 11, 13421-13449, [https://doi.org/10.5194/acp-11-](https://doi.org/10.5194/acp-11-13421-2011)
1296 13421-2011, 2011.

1297 Hirahara, S., Ishii, M., and Fukuda, Y.: Centennial-Scale Sea Surface Temperature
1298 Analysis and Its Uncertainty. *J. Climate*, 27, 57-75, [https://doi.org/10.1175/JCLI-D-](https://doi.org/10.1175/JCLI-D-12-00837.1)
1299 12-00837.1, 2014.

1300 Holte, J., Talley, L. D., Gilson, J., and Roemmich, D.: An Argo mixed layer climatology
1301 and database. *Geophys. Res. Lett.*, 44, 5618-5626,
1302 <https://doi.org/10.1002/2017GL073426>, 2017.

1303 Hosoda, S., Ohira, T., and Nakamura, T.: Monthly mean dataset of global oceanic
1304 temperature and salinity derived from Argo float observations. *JAMSTEC Report of*
1305 *Research and Development*, 8, <https://doi.org/10.5918/jamstecr.8.47>, 2008.

1306 Huang, B., Thorne, P. W., Banzon, V. F., Boyer, T., Chepurin, G., Lawrimore, J. H.,
1307 Menne, M. J., Smith, T. M., Vose, R. S., and Zhang, H.-M.: Extended Reconstructed
1308 Sea Surface Temperature, Version 5 (ERSSTv5): Upgrades, Validations, and
1309 Intercomparisons. *J. Climate*, 30, 8179-8205, [https://doi.org/10.1175/JCLI-D-16-](https://doi.org/10.1175/JCLI-D-16-0836.1)
1310 0836.1, 2017.

1311 Hugonnet, R., McNabb, R., Berthier, E., Menounos, B., Nuth, C., Girod, L., Farinotti, D.,
1312 Huss, M., Dussaillant, I., Brun, F., and Käab, A.: Accelerated global glacier mass
1313 loss in the early twenty-first century. *Nature*, 592, 726-731,
1314 <https://doi.org/10.1038/s41586-021-03436-z>, 2021.

1315 IPCC: Annex I: Observational Products [Trewin, B. (ed.)], pp. 2061–2086 pp. , 2021

1316 Ishii, M., and Kimoto, M.: Reevaluation of historical ocean heat content variations with
1317 time-varying XBT and MBT depth bias corrections. *J. Oceanogr.*, 65, 287-299,
1318 <https://doi.org/10.1007/s10872-009-0027-7>, 2009.

1319 Ishii, M., Shouji, A., Sugimoto, S., and Matsumoto, T.: Objective analyses of sea-surface
1320 temperature and marine meteorological variables for the 2⁰th century using ICOADS
1321 and the Kobe Collection. *Int. J. Climatol.*, 25, 865-879,
1322 <https://doi.org/10.1002/joc.1169>, 2005.

1323 Ishii, M., Y. Fukuda, S. Hirahara, S. Yasui, T. Suzuki, and K. Sato: Accuracy of Global
1324 Upper Ocean Heat Content Estimation Expected from Present Observational Data
1325 Sets. *Sola*, 13, 163-167, <https://doi.org/10.2151/sola.2017-030>, 2017.

1326 Jin, F.-F.: An Equatorial Ocean Recharge Paradigm for ENSO. Part I: Conceptual Model.
1327 J. Atmos. Sci., 54, 811-829, <https://doi.org/10.1175/1520->
1328 0469(1997)054%3C0811:AEORPF%3E2.0.CO;2, 1997.

1329 Jin, Y., Li, Y., Cheng, L., Duan, J., Li, R., & Wang, F.. Ocean heat content increase of the
1330 Maritime Continent since the 1990s. Geophysical Research Letters, 51,
1331 e2023GL107526. <https://doi.org/10.1029/2023GL107526>, 2024.

1332 Johns, W. E., Elipot, S., Smeed, D. A., Moat, B., King, B., Volkov, D. L., and Smith, R. H.:
1333 Towards two decades of Atlantic Ocean mass and heat transports at 26.5° N.
1334 Philosophical Transactions of the Royal Society A: Mathematical, Physical and
1335 Engineering Sciences, 381, 20220188, 2023.

1336 Johnson, G. C., Purkey, S. G., Zilberman, N. V., and Roemmich, D.: Deep Argo Quantifies
1337 Bottom Water Warming Rates in the Southwest Pacific Basin. Geophys. Res. Lett.,
1338 46, 2662-2669, <https://doi.org/10.1098/rsta.2022.0188>, 2019.

1339 Katsumata, K., Purkey, S. G., Cowley, R., Sloyan, B. M., Diggs, S. C., Moore, T. S.,
1340 Talley, L. D., and Swift, J. H.: GO-SHIP Easy Ocean: Gridded ship-based
1341 hydrographic section of temperature, salinity, and dissolved oxygen. Scientific Data,
1342 9, 103, <https://doi.org/10.1038/s41597-022-01212-w>, 2022.

1343 Kennedy, J.: A review of uncertainty in in situ measurements and data sets of sea surface
1344 temperature. Rev. Geophys., 52, 1-32, <https://doi.org/10.1002/2013RG000434>, 2014.

1345 Levitus, S., Antonov, J. I., Boyer, T. P., Locarnini, R. A., Garcia, H. E., and Mishonov, A.
1346 V.: Global ocean heat content 1955–2008 in light of recently revealed
1347 instrumentation problems. Geophys. Res. Lett., 36,
1348 <https://doi.org/10.1029/2008GL037155>, 2009

1349 Levitus, S., Antonov, J. I., Boyer, T. P., Baranova, O. K., Garcia, H. E., Locarnini, R. A.,
1350 Mishonov, A. V, Reagan, J. R., Seidov, D., Yarosh, E. S., and Zweng, M. M.: World
1351 ocean heat content and thermosteric sea level change (0–2000 m), 1955–2010,
1352 Geophys. Res. Lett., 39, L10603, <https://doi.org/10.1029/2012GL051106>, 2012.

1353 Li, G., Cheng, L., Zhu, J., Trenberth, K. E., Mann, M. E., and Abraham, J. P.: Increasing
1354 ocean stratification over the past half-century. Nat. Clim. Change, 10, 1116-1123,
1355 <https://doi.org/10.1038/s41558-020-00918-2>, 2020.

1356 Li, H., Xu, F., Zhou, W., Wang, D., Wright, J. S., Liu, Z., and Lin, Y.: Development of a
1357 global gridded Argo data set with Barnes successive corrections. J. Geophys. Res.
1358 Oceans, 122, 866-889, <https://doi.org/10.1002/2016JC012285>, 2017.

1359 Li, Y., Church, J. A., McDougall, T. J., and Barker, P. M.: Sensitivity of Observationally
1360 Based Estimates of Ocean Heat Content and Thermal Expansion to Vertical
1361 Interpolation Schemes. *Geophys. Res. Lett.*, 49, e2022GL101079,
1362 <https://doi.org/10.1029/2022GL101079>, 2022.

1363 Lian, T., Wang, J., Chen, D., Liu, T. and Wang, D.: A Strong 2023/24 El Niño is Staged by
1364 Tropical Pacific Ocean Heat Content Buildup. *Ocean-Land-Atmosphere Research*, 2,
1365 0011, <https://doi.org/10.34133/olar.0011>, 2023.

1366 Liu, C., and Allan, R.: Reconstructions of the radiation fluxes at the top of atmosphere and
1367 net surface energy flux: DEEP-C version 5.0. . a. A. University of Reading Dataset,
1368 Ed., <https://doi.org/10.17864/1947.000347>, 2022

1369 Liu, C., Allan, R. P., Mayer, M., Hyder, P., Loeb, N. G., Roberts, C. D., Valdivieso, M.,
1370 Edwards, J. M., and Vidale, P.-L.: Evaluation of satellite and reanalysis-based global
1371 net surface energy flux and uncertainty estimates. *J. Geophys. Res.- Atmospheres*,
1372 122, 6250-6272, <https://doi.org/10.1002/2017JD026616>, 2017.

1373 Liu, C., Allan, R. P., Mayer, M., Hyder, P., Desbruyères, D., Cheng, L., Xu, J., Xu, F., and
1374 Zhang, Y.: Variability in the global energy budget and transports 1985–2017, *Clim.*
1375 *Dynam.*, 55, 3381– 3396, <https://doi.org/10.1007/s00382-020-05451-8>, 2020.

1376 Loeb, N. G., B. A. Wielicki, D. R. Doelling, G. L. Smith, D. F. Keyes, S. Kato, N. Manalo-
1377 Smith, and T. Wong: Toward Optimal Closure of the Earth's Top-of-Atmosphere
1378 Radiation Budget. *J. Climate*, 22, 748–766, <https://doi.org/10.1175/2008JCLI2637.1>,
1379 2009.

1380 Loeb, N. G., Johnson, G. C., Thorsen, T. J., Lyman, J. M., Rose, F. G., and Kato, S.:
1381 Satellite and Ocean Data Reveal Marked Increase in Earth's Heating Rate. *Geophys.*
1382 *Res. Lett.*, 48, <https://doi.org/10.1029/2021gl093047>, 2021.

1383 Loeb, N. G., Thorsen, T. J., Norris, J. R., Wang, H., and Su, W.: Changes in Earth's energy
1384 budget during and after the “Pause” in global warming: An observational
1385 perspective, *Climate*, 6, 62, <https://doi.org/10.3390/cli6030062>, 2018.

1386 Lyman, J. M., and Johnson, G. C.: Estimating Global Ocean Heat Content Changes in the
1387 Upper 1800 m since 1950 and the Influence of Climatology Choice. *J. Climate*, 27,
1388 1945-1957, <https://doi.org/10.1175/JCLI-D-12-00752.1>, 2014.

1389 Lyman, J. M., Good, S. A., Gouretski, V. V., Ishii, M., Johnson, G. C., Palmer, M. D.,
1390 Smith, D. M., and Willis, J. K.: Robust warming of the global upper ocean. *Nature*,
1391 465, 334-337, <https://doi.org/10.1038/nature09043>, 2010.

1392 Lyman, J. M., and G. C. Johnson, 2023: Global High-Resolution Random Forest
1393 Regression Maps of Ocean Heat Content Anomalies Using In Situ and Satellite Data.
1394 J. Atmos. Oceanic Technol., 40, 575–586, [https://doi.org/10.1175/JTECH-D-22-](https://doi.org/10.1175/JTECH-D-22-0058.1)
1395 [0058.1](https://doi.org/10.1175/JTECH-D-22-0058.1).

1396 Mann, M.E., Beyond the Hockey Stick: Climate Lessons from The Common Era, Proc.
1397 Natl. Acad. Sci., 118 (39) e2112797118, <https://doi.org/10.1073/pnas.2112797118>,
1398 2021.

1399 McDougall T. J. and P. M. Barker, 2011: Getting started with TEOS-10 and the Gibbs
1400 Seawater (GSW) Oceanographic Toolbox, 28pp., SCOR/IAPSO WG127, ISBN 978-
1401 0-646-55621-5.

1402 Mayer, J., Mayer, M., and Haimberger, L.: Consistency and Homogeneity of Atmospheric
1403 Energy, Moisture, and Mass Budgets in ERA5. J. Climate, 34, 3955-3974,
1404 <https://doi.org/10.1175/JCLI-D-20-0676.1>, 2021.

1405 Mayer, M., Alonso Balmaseda, M., and Haimberger, L.: Unprecedented 2015/2016 Indo-
1406 Pacific Heat Transfer Speeds Up Tropical Pacific Heat Recharge. Geophys. Res.
1407 Lett., 45, 3274-3284, <https://doi.org/10.1002/2018GL077106>, 2018.

1408 Mayer, M., S. Tietsche, L. Haimberger, T. Tsubouchi, J. Mayer, and H. Zuo, 2019: An
1409 Improved Estimate of the Coupled Arctic Energy Budget. J. Climate, 32, 7915–7934,
1410 <https://doi.org/10.1175/JCLI-D-19-0233.1>.

1411 McPhaden, M. J.: A 2^{1st} century shift in the relationship between enso sst and warm water
1412 volume anomalies. Geophys. Res. Lett., 39, 9706,
1413 <https://doi.org/10.1029/2012GL051826>, 2012.

1414 McMahan, C. R., Roquet, F., Baudel, S., Belbeoch, M., Bestley, S., Blight, C., Boehme,
1415 L., Carse, F., Costa, D. P., Fedak, M. A., Guinet, C., Harcourt, R., Heslop, E.,
1416 Hindell, M. A., Hoenner, X., Holland, K., Holland, M., Jaime, F. R. A., Jeanniard du
1417 Dot, T., . . . Woodward: Animal Borne Ocean Sensors – AniBOS – An Essential
1418 Component of the Global Ocean Observing System. Front. Mar. Sci., 8,
1419 <https://doi.org/10.3389/fmars.2021.751840>, 2021.

1420 Meyssignac, B., Boyer, T., Zhao, Z., Hakuba, M. Z., Landerer, F. W., Stammer, D., Köhl,
1421 A., Kato, S., L’Ecuyer, T., Ablain, M., Abraham, J. P., Blazquez, A., Cazenave, A.,
1422 Church, J. A., Cowley, R., Cheng, L., Domingues, C. M., Giglio, D., Gouretski, V.,
1423 Ishii, M., Johnson, G. C., Killick, R. E., Legler, D., Llovel, W., Lyman, J., Palmer,
1424 M. D., Piotrowicz, S., Purkey, S. G., Roemmich, D., Roca, R., Savita, A.,
1425 Schuckmann, K. von, Speich, S., Stephens, G., Wang, G., Wijffels, S. E., and

1426 Zilberman, N.: Measuring Global Ocean Heat Content to Es-
1427 timate the Earth Energy Imbalance, *Front. Mar. Sci.*, 6, 432, <https://doi.org/10.3389/fmars.2019.00432>, 2019.

1428 Minière, A., von Schuckmann, K., Sallée, J.-B., and Vogt, L.: Robust acceleration of Earth
1429 system heating observed over the past six decades. *Sci. Rep.*, 13, 22975,
1430 <https://doi.org/10.1038/s41598-023-49353-1>, 2024

1431 Nerem, R. S., Beckley, B. D., Fasullo, J. T., Hamlington, B. D., Masters, D., and Mitchum,
1432 G. T.: Climate-change–driven accelerated sea-level rise detected in the altimeter era.
1433 *P. Natl. Acad. Sci.*, 115, 2022–2025, <https://doi.org/10.1073/pnas.1717312115>, 2018.

1434 O’Carroll, A. G., Armstrong, E. M., Beggs, H. M., Bouali, M., Casey, K. S., Corlett, G. K.,
1435 Dash, P., Donlon, C. J., Gentemann, C. L., Høyer, J. L., Ignatov, A., Kabobah, K.,
1436 Kachi, M., Kurihara, Y., Karagali, I., Maturi, E., Merchant, C. J., Marullo, S.,
1437 Minnett, P. J., Pennybacker, M., Ramakrishnan, B., Ramsankaran, R. Santoleri, R.,
1438 Sunder, S., Saux Picart, S. Vázquez-Cuervo, J., Wimmer, W.: Observational Needs
1439 of Sea Surface Temperature. *Front. Mar. Sci.*, 6,
1440 <https://doi.org/10.3389/fmars.2019.00420>, 2019.

1441 Oliver, E. C. J., Benthuisen, J.A., Darmaraki, S., Donat, M. G., Hobday, A. J., Holbrook,
1442 N. J., Schlegel, R.W., and Sen Gupta A., Marine Heatwaves. *Annual review of*
1443 *marine science* **13**, 313–342, [https://doi.org/10.1146/annurev-marine-032720-](https://doi.org/10.1146/annurev-marine-032720-095144)
1444 [095144](https://doi.org/10.1146/annurev-marine-032720-095144), 2021.

1445 Purkey, S. G., and Johnson, G. C.: Warming of Global Abyssal and Deep Southern Ocean
1446 Waters between the 1990s and 2000s: Contributions to Global Heat and Sea Level
1447 Rise Budgets. *J. Climate*, 23, 6336–6351, <https://doi.org/10.1175/2010jcli3682.1>,
1448 2010.

1449 Palmer, M. D., and K. Haines: Estimating Oceanic Heat Content Change Using Isotherms.
1450 *J. Climate*, 22, 4953–4969, <https://doi.org/10.1175/2009JCLI2823.1>, 2009.

1451 Rahmstorf, S., Box, J., Feulner, G., Mann, M.E., Robinson, A., Rutherford, S.,
1452 Schaffernicht, E. Exceptional 2⁰h-Century slowdown in Atlantic Ocean
1453 overturning, *Nature Climate Change*, 5, 475–480, 2015.

1454 Rayner, N. A., Parker, D. E., Horton, E. B., Folland, C. K., Alexander, L. V., Rowell, D.
1455 P., Kent, E. C., and Kaplan, A.: Global analyses of sea surface temperature, sea ice,
1456 and night marine air temperature since the late nineteenth century. *J. Geophys. Res.-*
1457 *Atmospheres*, 108, <https://doi.org/https://doi.org/10.1029/2002JD002670>, 2003.

1458 Reiniger, R. F., and Ross, C. K.: A method of interpolation with application to
1459 oceanographic data. *Deep Sea Research*, 15, 185-193, [https://doi.org/10.1016/0011-](https://doi.org/10.1016/0011-7471(68)90040-5)
1460 [7471\(68\)90040-5](https://doi.org/10.1016/0011-7471(68)90040-5), 1968.

1461 Rhein, M., S.R. Rintoul, S. Aoki, E. Campos, D. Chambers, R.A. Feely, S. Gulev, G.C.
1462 Johnson, S.A. Josey, A. Kostianoy, C. Mauritzen, D. Roemmich, L.D. Talley and F.
1463 Wang, 2013: Observations: Ocean. In: *Climate Change 2013: The Physical Science*
1464 *Basis. Contribution of Working Group I to the Fifth Assessment Report of the*
1465 *Intergovernmental Panel on Climate Change* [Stocker, T.F., D. Qin, G.-K. Plattner,
1466 M. Tignor, S.K. Allen, J. Boschung, A. Nauels, Y. Xia, V. Bex and P.M. Midgley
1467 (eds.)]. Cambridge University Press, Cambridge, United Kingdom and New York,
1468 NY, USA.

1469 Roemmich, D., and Gilson, J.: The 2004–2008 mean and annual cycle of temperature,
1470 salinity, and steric height in the global ocean from the Argo Program. *Prog.*
1471 *Oceanogr.*, 82, 81-100, <https://doi.org/10.1016/j.pocean.2009.03.004>, 2009.

1472 Roemmich, D., and Gilson, J.: The global ocean imprint of ENSO. *Geophys. Res. Lett.*, 38,
1473 <https://doi.org/10.1029/2011GL047992>, 2011.

1474 Roemmich, D., Alford, M. H., Claustre, H., Johnson, K., King, B., Moum, J., Oke, P.,
1475 Owens, W. B., Pouliquen, S., Purkey, S., Scanderbeg, M., Suga, T., Wijffels, S.,
1476 Zilberman, N., Bakker, D., Baringer, M., Belbeoch, M., Bittig, H. C., Boss, E., . . .
1477 Yasuda, I.: On the Future of Argo: A Global, Full-Depth, Multi-Disciplinary Array.
1478 *Front. Mar. Sci.*, 6, 2019.

1479 Savita, A., and Coauthors: Quantifying Spread in Spatiotemporal Changes of Upper-Ocean
1480 Heat Content Estimates: An Internationally Coordinated Comparison. *J. Climate*, 35,
1481 851–875, <https://doi.org/10.1175/JCLI-D-20-0603.1>, 2022.

1482 Schweiger, A., R. Lindsay, J. Zhang, M. Steele, H. Stern, and R. Kwok: Uncertainty in
1483 modeled Arctic sea ice volume. *J. Geophys. Res.*, 116, C00D06,
1484 <https://doi.org/10.1029/2011JC007084>, 2011.

1485 Sloyan, B. M., Wanninkhof, R., Kramp, M., Johnson, G. C., Talley, L. D., Tanhua, T.,
1486 McDonagh, E., Cusack, C., O'Rourke, E., McGovern, E., Katsumata, K., Diggs, S.,
1487 Hummon, J., Ishii, M., Azetsu-Scott, K., Boss, E., Ansorge, I., Perez, F. F., Mercier,
1488 H., . . . Campos, E.: The Global Ocean Ship-Based Hydrographic Investigations
1489 Program (GO-SHIP): A Platform for Integrated Multidisciplinary Ocean Science.
1490 *Front. Mar. Sci.*, 6, 2019.

1491 Sun, D., Li, F., Jing, Z. et al. Frequent marine heatwaves hidden below the surface of the
1492 global ocean. *Nat. Geosci.* 16, 1099–1104, [https://doi.org/10.1038/s41561-023-](https://doi.org/10.1038/s41561-023-01325-w)
1493 01325-w, 2023.

1494 Su, H. et al. OPEN: a new estimation of global ocean heat content for upper 2000 meters
1495 from remote sensing data. *Remote Sens*, <https://doi.org/10.3390/rs12142294>, 2020.

1496 Tan, Z., Zhang, B., Wu, X., Dong, M., and Cheng, L.: Quality control for ocean
1497 observations: From present to future. *Science China Earth Sciences*, 65, 215-233,
1498 <https://doi.org/10.1007/s11430-021-9846-7>, 2022.

1499 Tan, Z., Cheng, L., Gouretski, V., Zhang, B., Wang, Y., Li, F., Liu, Z., & Zhu, J.: A new
1500 automatic quality control system for ocean profile observations and impact on ocean
1501 warming estimate. *Deep Sea Research Part I: Oceanographic Research Papers*, 194,
1502 103961, <https://doi.org/10.1016/j.dsr.2022.103961>, 2023.

1503 Trenberth, K. E.: *The Changing Flow of Energy Through the Climate System*.
1504 Cambridge University Press., <https://doi.org/10.1017/9781108979030>, 2022.

1505 Trenberth, K. E., and Fasullo, J. T.: Atlantic meridional heat transports computed from
1506 balancing Earth's energy locally. *Geophys. Res. Lett.*, 44, 1919-1927,
1507 <https://doi.org/10.1002/2016gl072475>, 2017.

1508 Trenberth, K. E., Fasullo, J. T., and Kiehl, J.: Earth's Global Energy Budget *Bull. Am.*
1509 *Meteorol. Soc.*, 90, 311-324, <https://doi.org/10.1175/2008bams2634.1>, 2009.

1510 Trenberth, K. E., Fasullo, J. T., Von Schuckmann, K., and Cheng, L.: Insights into Earth's
1511 Energy Imbalance from Multiple Sources. *J. Climate*, 29, 7495-7505,
1512 <https://doi.org/10.1175/jcli-d-16-0339.1>, 2016.

1513 Trenberth, K. E., Zhang, Y., Fasullo, J. T., and Cheng, L.: Observation-Based Estimates of
1514 Global and Basin Ocean Meridional Heat Transport Time Series. *J. Climate*, 32,
1515 4567-4583, <https://doi.org/10.1175/jcli-d-18-0872.1>, 2019.

1516 von Schuckmann, K., and Le Traon, P. Y.: How well can we derive Global Ocean
1517 Indicators from Argo data? *Ocean Sci.*, 7, 783-791, [https://doi.org/10.5194/os-7-783-](https://doi.org/10.5194/os-7-783-2011)
1518 2011, 2011.

1519 von Schuckmann, K., Cheng, L., Palmer, M. D., Hansen, J., Tassone, C., Aich, V.,
1520 Adusumilli, S., Beltrami, H., Boyer, T., Cuesta-Valero, F. J., Desbruyères, D.,
1521 Domingues, C., García-García, A., Gentine, P., Gilson, J., Gorfer, M., Haim-berger,
1522 L., Ishii, M., Johnson, G. C., Killick, R., King, B. A., Kirchengast, G.,
1523 Kolodziejczyk, N., Lyman, J., Marzeion, B., Mayer, M., Monier, M., Monselesan, D.
1524 P., Purkey, S., Roemmich, D., Schweiger, A., Seneviratne, S. I., Shepherd, A., Slater,

1525 D. A., Steiner, A. K., Straneo, F., Timmermans, M.-L., and Wijffels, S. E.: Heat
1526 stored in the Earth system: where does the energy go?, *Earth Syst. Sci. Data*, 12,
1527 2013–2041, <https://doi.org/10.5194/essd-12-2013-2020>, 2020.

1528 von Schuckmann, K., Palmer, M. D., Trenberth, K. E., Cazenave, A., Chambers, D.,
1529 Champollion, N., Hansen, J., Josey, S. A., Loeb, N., Mathieu, P.-P., Meyssignac, B.,
1530 and Wild, M.: An imperative to monitor Earth’s energy imbalance, *Nat. Clim.*
1531 *Change*, 6, 138–144, <https://doi.org/10.1038/nclimate2876>, 2016.

1532 von Schuckmann, K. Minière, A. Gues, F. Cuesta-Valero, F. J. Kirchengast, G.
1533 Adusumilli, S. Straneo, F. Ablain, M. Allan, R. P. Barker, P. M. Beltrami, H.
1534 Blazquez, A. Boyer, T. Cheng, L. Church, J. Desbruyeres, D. Dolman, H.
1535 Domingues, C. M. García-García, A. Giglio, D. Gilson, J. E. Gorfer, M. Haimberger,
1536 L. Hakuba, M. Z. Hendricks, S. Hosoda, S. Johnson, G. C. Killick, R. King, B.
1537 Kolodziejczyk, N. Korosov, A. Krinner, G. Kuusela, M. Landerer, F. W. Langer, M.
1538 Lavergne, T. Lawrence, I. Li, Y. Lyman, J. Marti, F. Marzeion, B. Mayer, M.
1539 MacDougall, A. H. McDougall, T. Monselesan, D. P. Nitzbon, J. Otsuka, I. Peng, J.
1540 Purkey, S. Roemmich, D. Sato, K. Sato, K. Savita, A. Schweiger, A. Shepherd, A.
1541 Seneviratne, S. I. Simons, L. Slater, D. A. Slater, T. Steiner, A. K. Suga, T. Szekely,
1542 T. Thiery, W. Timmermans, M. L. Vanderkelen, I. Wjiffels, S. E. Wu, T. Zemp, M.:
1543 Heat stored in the Earth system 1960–2020: where does the energy go? *Earth Syst.*
1544 *Sci. Data*, 15, 1675-1709, <https://doi.org/10.5194/essd-15-1675-2023>, 2023.

1545 Wang, F., Shen, Y., Chen, Q., and Sun, Y.: Reduced misclosure of global sea-level budget
1546 with updated Tongji-Grace2018 solution. *Sci Rep-Uk*, 11, 17667,
1547 <https://doi.org/10.1038/s41598-021-96880-w>, 2021.

1548 Watkins, M. M., Wiese, D. N., Yuan, D. N., Boening, C., and Landerer, F. W.: Improved
1549 methods for observing Earth's time variable mass distribution with GRACE using
1550 spherical cap mascons. *J. Geophys. Res.- Solid Earth*, 120, 2648-2671,
1551 <https://doi.org/10.1002/2014JB011547>, 2015.

1552 Wijffels, S. E., Willis, J., Domingues, C. M., Barker, P., White, N. J., Gronell, A.,
1553 Ridgway, K., and Church, J. A.: Changing Expendable Bathythermograph Fall Rates
1554 and Their Impact on Estimates of Thermosteric Sea Level Rise. *J. Climate*, 21, 5657-
1555 5672, <https://doi.org/10.1175/2008jcli2290.1>, 2008.

1556 WMO: State of the Global Climate 2021, WMO-No. 1290, 2022.

1557 Wong, A. P. S., Wijffels, S. E., Riser, S. C., et al.: Argo Data 1999–2019: Two Million
1558 Temperature-Salinity Profiles and Subsurface Velocity Observations From a Global
1559 Array of Profiling Floats, <https://doi.org/10.3389/fmars.2020.00700>, 2020.

1560 Zanna, L., Khatiwala, S., Gregory, J. M., Ison, J. & Heimbach, P. Global reconstruction of
1561 historical ocean heat storage and transport. *Proc. Natl Acad. Sci. USA* 116, 1126–
1562 1131, <https://doi.org/10.1073/pnas.1808838115>, 2019.

1563 Zhang, B. et al. CAS-Ocean Data Center, Global Ocean Science Database (CODCv1):
1564 temperature. Marine Science Data Center of the Chinese Academy of Science,
1565 [doi:10.12157/IOCAS.20230525.001](https://doi.org/10.12157/IOCAS.20230525.001) (2024).

1566 Zhang, X., Church, J. A., Platten, S. M., and Monselesan, D.: Projection of subtropical
1567 gyre circulation and associated sea level changes in the Pacific based on CMIP3
1568 climate models. *Clim. Dyn.*, 43, 131-144, [https://doi.org/10.1007/s00382-013-1902-](https://doi.org/10.1007/s00382-013-1902-x)
1569 [x](https://doi.org/10.1007/s00382-013-1902-x), 2014.

1570